

.....  
Unterschrift des Betreuers



TECHNISCHE  
UNIVERSITÄT  
WIEN  
Vienna University of Technology

DIPLOMARBEIT

# Selective Internal Radiotherapy - Determination of the $^{90}\text{Y}$ Biodistribution using Computer Simulation of PET

Ausgeführt am Institut für Angewandte Physik der  
Technischen Universität Wien

Unter der Anleitung von Ao.Univ.-Prof. Dr. Martin Gröschl  
und Dr. Albert Hirtl als verantwortlich mitwirkendem  
Universitätsassistenten

durch

Johannes Anderl

Traviatagasse 21-29/6/3

1230 Wien

.....  
Datum

.....  
Unterschrift (Student)



# Vielen Dank!

Vor allem möchte ich mich bei Albert Hirtl bedanken, der nicht nur die Idee zu dieser Diplomarbeit hatte, sondern mir auch während der gesamten Zeit unterstützend zur Seite stand. Von ihm konnte ich viel in Bezug auf wissenschaftliches Arbeiten lernen, aber auch die Gespräche abseits von Wissenschaft waren mir immer ein Vergnügen und eine willkommene Abwechslung bei der Entstehung dieser Arbeit.

Ausserdem gilt mein Dank Prof. Martin Gröschl für die Betreuung und die gute Zusammenarbeit während der gesamten Entstehungszeit.

Danke auch an Ivo Rausch, der mir viele Tips und Tricks aus den Erfahrungen seiner Diplomarbeit weitergeben konnte, und so auch wesentlich am Entstehen dieser Arbeit beteiligt war.

Besonders danken möchte ich meinen Eltern und meiner Schwester Maria, die mich während des gesamten Studiums begleitet haben. Mit ihnen konnte ich viele freudige Momente teilen, aber auch bei Rückschlägen haben sie mir immer den Weg nach vorne gezeigt.

Danke auch an Andi, Manuel, Markus<sup>2</sup>, Michi, Sid,... für die viele Zeit während des Studiums, in der ihr mich vom Lernen abgehalten habt. :)



# Abstract

## Background

Selective Internal Radiotherapy (SIRT) has become a popular treatment against non-resective liver tumours.  $^{90}\text{Y}$  microspheres are used to deposit high energetic  $\beta^-$  radiation in the tumour cells, simultaneously cutting them off their blood supply. While studies have shown an improvement in life expectancy with these patients, the efficiency related to the radioactive impact on healthy human tissue is still not resolved. In the past, Bremsstrahlung was used to examine the dose distribution in the liver, however it suffers from a bad image resolution.

Besides  $\beta^-$  decay,  $^{90}\text{Y}$  has also got a small branch to the  $0^+$  first excited state of stable  $^{90}\text{Zr}$ , which is followed by internal electron positron pair production. Per MBq of  $^{90}\text{Y}$  decay, approximately 32 positrons are emitted [1, 2]. Therefore, positron emission tomography (PET) imaging offers the potential for improved image quality, allowing a more detailed examination of SIRT efficiency.

The aim of this diploma thesis is to design a computer based simulation model for  $^{90}\text{Y}$  PET imaging for a PET system currently present at the MedUni Vienna. Additionally, the impact of the settings for image reconstruction on the reconstructed image using filtered back projection (FBP) and iterative reconstruction was examined.

## Material and Methods

As a guideline for the PET set up, technical data from the Siemens TruePoint PET/CT were used. The phantom simulated was, to a high extent, based on the NEMA IEC body phantom which consists of 6 spherical sources of volumes 0.52, 1.15, 2.57, 5.58, 11.49 and 26.50 ml surrounded by a body shaped water phantom. This was approximated by a cylindrical shaped phantom.

Geant 4 Application for Tomographic Emission (GATE) was used for the PET simulation, including technical data of the PET device, information on the source and phantom, as well as on the relevant physical interactions. The computationally intensive simulations were executed in a computer grid present at the MedUni Vienna, combining the processor powers of several computers.

For the subsequent image reconstruction the gained simulation raw data had to be modi-

---

fied with a C++ source code, generously provided by a collaborating research group from Jülich. The FBP as well as the iterative reconstruction method was handled with STIR (Software for Tomographic Image Reconstruction). For visualisation and further image processing ImageJ was used.

## Results

The gained data from the  $^{18}\text{F}$  and  $^{90}\text{Y}$  simulation proofed the functionality of the PET simulation set up, respective to the energy distribution of the coincidence photons and the source location.

In this work no attenuation correction was applied in image reconstruction. The positron energy distribution of the  $^{90}\text{Y}$  decay was approximated by a mean positron energy value of 369 keV.

$^{18}\text{F}$  image reconstruction with a specific activity of 20 kBq/ml and a measurement time of 30 minutes showed acceptable image results for FBP and good results for the iterative reconstruction method (4 iterations, 12 subsets) leading to an excellent local resolution of the single sources.

$^{90}\text{Y}$  image reconstruction exhibited an expected degradation in image quality compared to  $^{18}\text{F}$  due to a decrease in sensitivity by a factor of  $10^{-5}$  [3]. FBP showed bad results for 4 MBq/ml and acceptable results for 40 MBq/ml. With iterative reconstruction and a specific activity of 40 MBq/ml all the sources could be identified, leading to a good image quality. Iterative reconstruction with a realistic specific activity of 4 MBq/ml and a background activity of 0.5 MBq/ml led to a worse image quality. Still, 5 out of 6 sources could be identified. Real  $^{90}\text{Y}$  PET phantom measurements showed similar results concerning image quality.

## Conclusion and Outlook

The process of PET imaging and subsequent image reconstruction on the basis of a computer simulation was set up, successfully completing both the  $^{18}\text{F}$  and  $^{90}\text{Y}$  PET simulation. The results clearly showed the difference in image quality between these two nuclides, and the potential of PET imaging for the determination of the  $^{90}\text{Y}$  biodistribution in SIRT. Considering attenuation and scatter correction will improve image quality and must be included in a further work. Measured CT and PET data could serve as basis for a simulation in GATE, allowing the determination of the dose distribution in the liver.

# Contents

<b>1</b>	<b>Introduction and Motivation</b>	<b>1</b>
<b>2</b>	<b>Basics of Clinical Nuclear Imaging</b>	<b>3</b>
2.1	Nuclear Medicine . . . . .	3
2.1.1	History . . . . .	3
2.1.2	SIRT - Selective Internal Radiotherapy . . . . .	4
2.1.3	Imaging Techniques . . . . .	5
2.2	Medical Radiation Physics . . . . .	7
2.2.1	Radioactive Decay . . . . .	9
2.2.2	Nuclide Production . . . . .	15
2.2.3	Photon Interaction with Matter . . . . .	16
2.2.4	Attenuation of Photons . . . . .	21
2.3	PET/CT - Positron Emission Tomography/Computed Tomography . . . . .	22
2.3.1	Basic Functionality . . . . .	23
2.3.2	Scanner Design . . . . .	23
2.3.3	Detectors . . . . .	23
2.3.4	Types of Coincidences . . . . .	24
2.3.5	Spatial Resolution . . . . .	26
2.3.6	Attenuation Correction . . . . .	28
2.3.7	Data Representation - Sinogram . . . . .	29
2.4	Image Reconstruction . . . . .	30
2.4.1	Filtered Back Projection . . . . .	31
2.4.2	Iterative Reconstruction . . . . .	31
<b>3</b>	<b>Materials and Methods</b>	<b>35</b>
3.1	Siemens TruePoint PET/CT . . . . .	35
3.2	Source and Phantom . . . . .	35

3.3	PET Simulation . . . . .	37
3.3.1	GATE . . . . .	37
3.3.2	Grid . . . . .	38
3.4	Image Reconstruction . . . . .	38
3.4.1	Data Manipulation . . . . .	38
3.4.2	STIR . . . . .	39
3.5	Image Visualisation . . . . .	40
3.5.1	ImageJ . . . . .	40
<b>4</b>	<b>Simulation and Image Reconstruction</b>	<b>41</b>
4.1	PET Simulation - GATE . . . . .	41
4.1.1	Submitting Simulation to Grid . . . . .	47
4.2	Image Reconstruction - STIR . . . . .	47
<b>5</b>	<b>Results and Discussion</b>	<b>49</b>
5.1	Fluorine 18 . . . . .	49
5.1.1	Simulation . . . . .	49
5.1.2	Image Reconstruction . . . . .	52
5.2	Yttrium 90 . . . . .	60
5.2.1	Simulation . . . . .	60
5.2.2	Image Reconstruction . . . . .	64
<b>6</b>	<b>Y90 - Phantom Measurements</b>	<b>69</b>
<b>7</b>	<b>Summary and Outlook</b>	<b>73</b>
<b>A</b>	<b>Image Reconstruction - STIR</b>	<b>75</b>
A.1	User Manual . . . . .	75





# 1 Introduction and Motivation

The field of nuclear medicine reveals a synergy between the sciences of physics and medicine. Medical imaging and therapy profits from the consideration of physical mechanisms. The combination of applied physics and medicine is the main topic in this diploma thesis. Selective internal radiotherapy (SIRT) is a practical example for the benefit of physical know-how in medicine. This therapy form, that has been applied recently for non-resectable liver tumours, uses the high energetic radioactive  $\beta^-$  decay (2.28 MeV) of  $^{90}\text{Y}$  microspheres to treat hepatocellular cancer.

Even though SIRT is applied successfully, the efficiency of this method is still under examination since the quantitative uptake and impact of the  $^{90}\text{Y}$  microspheres on healthy human body cells is not completely resolved yet.

Bremsstrahlung detectable with SPECT (Single Photon Emission Computed Tomography) is commonly used to image the  $^{90}\text{Y}$  uptake by the liver but suffers from a bad resolution. A promising alternative to Bremsstrahlung, concerning image resolution, is PET imaging.  $^{90}\text{Y}$ , mainly a  $\beta^-$  emitter, also has a small branch to the first excited state ( $0^+$ ) of  $^{90}\text{Zr}$ . The electromagnetic transition from this excited state to the ground state ( $0^+$ ) is forbidden for quantum mechanical reasons since it is a spin-zero to spin-zero transition. As an alternative process internal pair production may occur. The probability of electron positron pair production in  $^{90}\text{Y}$   $\beta^-$  decay is  $3.2 \cdot 10^{-5}$  [1,2]. The generated positrons can form a PET signal after an electron positron annihilation.

Several studies have shown the possible advantages of  $^{90}\text{Y}$  PET imaging in comparison to Bremsstrahlung [2–7]. At the same noise level PET images show a higher contrast than the corresponding SPECT images [2] (see figure 1.1).

The aim of this thesis is to set up a Monte Carlo model for a more detailed analysis of the  $^{90}\text{Y}$  bio distribution on basis of PET imaging. Since research facilities and accessible devices in daily clinical routine are limited, computer simulations offer a promising alternative for the examination of many technical issues in medicine. For this reason a

computer model of a PET currently present at the MedUni Vienna was assembled. Furthermore, different image reconstruction techniques were investigated and compared.

To give the reader an impression of the content and structure of this diploma thesis, a short summary of the sections is given:

In chapter 2, a theoretical description of the most important topics in this thesis is presented. It gives a short introduction to nuclear medicine with a focus on SIRT. The basics of nuclear physics are explained as well as the functionality of common nuclear imaging techniques, especially PET, along with a brief discussion of different image reconstruction methods.

Chapter 3 gives a comprehensive overview on the programs and methods used for the simulation, data manipulation and image reconstruction.

In chapter 4, the individual steps starting from the simulation set up to the final image are described. This contains detailed information about the simulation structure and the process of reconstructing the image. The belonging source codes and further information can be found on an external disk and in the appendix, respectively.

Results, together with a discussion on the used simulations are shown in chapter 5.

Phantom measurements performed by a research group at MedUni Vienna are presented in chapter 6.

Chapter 7 serves as a summary of the most important results and gives an outlook on further possible investigations based on this thesis.

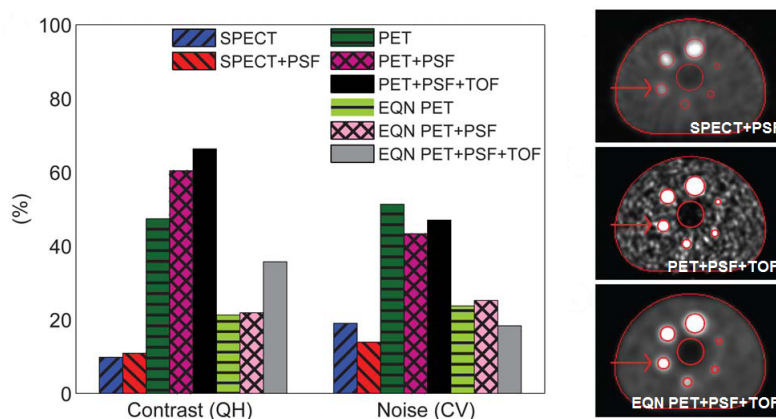


**Figure 1.1:** Comparison of PET and SPECT image contrast and noise. The equal noise (EQN) PET mode was reconstructed with SPECT-like noise level and shows a higher contrast than the SPECT mode [2].

# 2 Basics of Clinical Nuclear Imaging

## 2.1 Nuclear Medicine

Prospects of the interaction of physics and medicine reveal a multitude of technical opportunities concerning imaging and therapy forms like it is used for liver cancer treatment. In this section, a short extract of some of the historical milestones in nuclear medicine is given. Selective Internal Radiotherapy (SIRT) is explained in more detail since it is of major importance in this diploma thesis. Commonly used imaging techniques in nuclear medicine are described.

### 2.1.1 History

The history of nuclear medicine started with the discovery of radioactivity by Henri Becquerel in 1896. Without knowing at this point, this turned out to be marking the beginning of a rapidly growing field of research.

George de Hevesy was the first to use the tracer principle by injecting a radioactive isotope into rats displaying their metabolic pathways in 1923.

A few years later, in 1926, Blumgart started to examine the blood flow in a human body by injecting a tracer substance ( $^{212}\text{Bi}$ ) into the left arm of a patient and measuring the elapsed time until the activity could be indicated in the other arm.

With the discovery of induced radioactivity by Irene and Frederic Joliot in 1934 the modern time of nuclear medicine began.

In 1938 the first investigations on thyroid diagnostics with  $^{131}\text{I}$  were carried out and the first thyroid disorder treatment was performed in 1942.

The development of nuclear reactors in the early 1940's and the production of several new radioactive isotopes within these reactors in the 1950's led to further inventions like the Anger camera by Hal Anger in 1958.

Around 1970 the first mathematical algorithms used for image reconstructions were de-

veloped.

The effort in mathematical know-how concerning image reconstruction as well as advanced computation capacities led to the tomographic concepts of modern Single Photon Emission Computed Tomography (SPECT) and Positron Emission Tomography (PET).

### 2.1.2 SIRT - Selective Internal Radiotherapy

Selective Internal Radiotherapy (SIRT) is a cancer treatment method for non-resectable tumours like hepatocellular (HCC) cancer in the liver. SIRT has been introduced and applied since other therapy forms using external beam radiation like chemotherapy did not show great success in liver cancer treatment by reason of the poor tolerance of the liver to external radiation.

In SIRT,  $^{90}\text{Y}$  microspheres with a diameter of approximately  $35\ \mu\text{m}$  are injected into the hepatic artery which is the main blood supply for tumours present in the liver. In contrast to this, the normal liver parenchyma is predominantly supplied by the portal vein. This provides a selective uptake primarily into the hepatic tumours with only little penetration into the healthy liver tissue. A visualization of SIRT is given in figure 2.1.

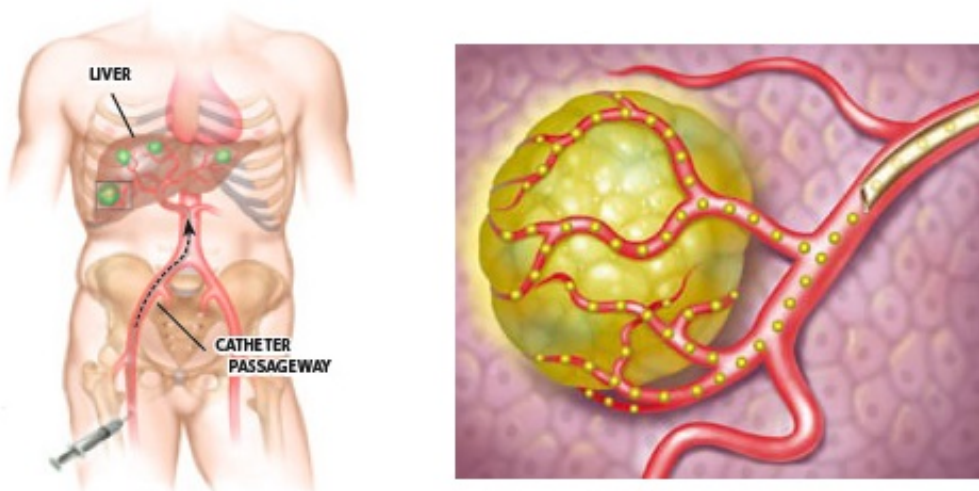


**Figure 2.1:** Visualization of SIRT. Left: The  $^{90}\text{Y}$  microspheres are injected into the hepatic artery where they are transferred to the tumour cells in the liver. Right: Microspheres get stuck in the tiny blood vessels, cutting the tumour off the blood supply and deposit high energetic  $\beta^-$  particles [8], [9].

The functionality of  $^{90}\text{Y}$  microspheres is given by two main factors:

The  $35\ \mu\text{m}$  microspheres get stuck in the tiny blood vessels supplying the tumour. Thereby, a large part of the tumour is cut off from the blood supply. The second factor is based on the high energetic  $\beta^-$  decay (2.28 MeV) of  $^{90}\text{Y}$ , meant to destroy the tumour cells. This is also called radioembolisation. Since these  $\beta^-$  particles have a range of about 10 mm, healthy liver tissue is not affected a lot. Despite this, the effective damage of normal liver tissue is still under research.

### 2.1.3 Imaging Techniques

Imaging in nuclear medicine is essential since it provides an insight into the human body and is therefore indispensable for diagnosis and further patient treatment.

On the basis of the importance of appropriate imaging methods in medicine, an overview of frequently used imaging techniques is given. For further information on imaging techniques in the field of nuclear medicine the reader is referred to literature [10].

**Gamma Camera** This device is used, as the name reveals, to detect and locate electromagnetic radiation originating from  $\gamma$  decay. Radionuclides emitting gamma rays within the energy range of 100 – 300 keV can be displayed efficiently with this method. This includes the commonly used radioactive substances iodine and technetium.

In principle a gamma camera consists of a collimator, a scintillating crystal (commonly Sodium Iodine (NaI(Tl)) and photomultiplier tubes (see figure 2.2). The collimator ensures that only photons perpendicular or within a certain angle of acceptance to the scintillating crystal are taken into consideration. The crystal converts the high energetic photons into visible light, leading to a higher detection efficiency. The photons are then passed on to the photomultiplier tubes where an electrical signal is formed and amplified.

**Single Photon Emission Tomography** Single Photon Emission Computed Tomography (SPECT) uses the detection method of a gamma camera as its tomographic application. For 3D imaging the gamma camera is rotated along a circle with different projection planes. A rotation angle of  $180^\circ$  is sufficient for image reconstruction.  $360^\circ$  projection data recording still has advantages in terms of resolution and attenuation correction. An illustration of a SPECT system with corresponding projection planes can be found in figure 2.3.



**Figure 2.2:** Picture of a gamma camera present at the MedUni Vienna. The two gamma camera blocks are rotated around the patient for 3D imaging [Figure: Courtesy of A. Hirtl].

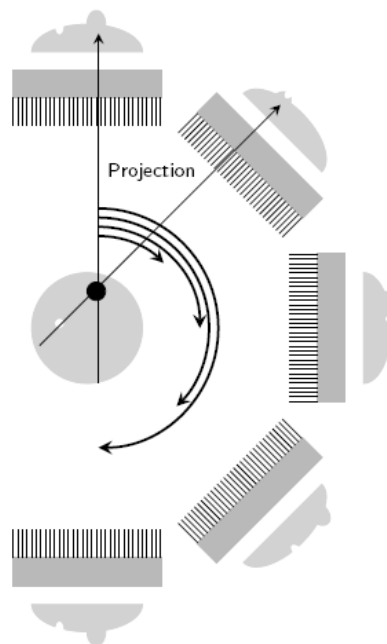


**Figure 2.3:** Schematic picture of a SPECT with corresponding projection planes [Figure: Courtesy of A. Hirtl].

**Positron Emission Tomography** Positron Emission Tomography (PET) as a highly sensitive nuclear imaging device detects photon pairs in coincidence originating from an annihilation process to locate a radioactive source. Even though the principle of PET imaging is very simple, the implementing in reality bares a lot of necessary and detailed know-how. Due to the importance of PET in this diploma thesis, its basics are described in more detail in section 2.3.

## 2.2 Medical Radiation Physics

The theoretical descriptions in this section are, to a high extent, based on the literature *Grundlagen der Strahlungsphysik und des Strahlenschutzes* by Hanno Krieger [11].

Common physical processes one benefits from in the field of medical radiation physics occur on an atomic level. An atom consists of a positively charged nucleus containing protons and neutrons surrounded by a negatively charged electron cloud. Although the nucleus is almost punctual compared to the atomic shell, the mass of an atom is basically carried by the nucleus, since nucleons are about 2000 times heavier than electrons. The electrons of an atom exist in discrete orbitals which correspond to their energetic state. The attraction between the protons located in the nucleus and the electrons surrounding the nucleus is based on the electromagnetic force, described by quantum electrodynamics (QED).

The stability of the nucleus cannot be explained simply by the electromagnetic force, since positively charged protons repel each other from an electrostatic point of view. Therefore other forces have to be considered: The strong force, which is important for the binding of the nucleus, and the weak force, which is responsible for the  $\beta$  decay. The quantum field theory for describing the binding of the nucleons as well as the properties of their sub-particles, the quarks, is called quantum chromodynamics (QCD).

A detailed quantum theoretical treatment of the interactions taking place in a nucleus is very complicated and requires complex mathematical models which, in many cases, cannot be solved analytically. Therefore numerical methods are needed.

Besides the theoretical description within quantum physics there exist other, more simple methods to describe the stability of a nucleus. One of them is the semi-empirical Bethe-Weizsäcker formula. Even though it cannot explain all characteristics of a nucleus, like excited nucleus states, it provides good results for the calculation of the binding energy

of a nucleus which is an indicator for the core stability.

The Bethe-Weizsäcker formula, also known as the liquid drop model, assumes that the nucleons behave like particles in a liquid drop. It implies 5 terms adding up to the overall binding energy:

1. The volume term:

$$E_{\text{Cond}} = a_V \cdot A \approx 15.85 \text{ MeV} \cdot A.$$

In this term,  $E_{\text{Cond}}$  stands for the condensation energy of particles in a liquid with given volume  $V$ . The volume is proportional to the number of particles  $A$  and  $a_V$  is an empirically determined proportional constant.

2. The surface term:

$$E_{\text{Sur}} = -a_{\text{Sur}} \cdot A^{\frac{2}{3}} \approx -18.34 \text{ MeV} \cdot A^{\frac{2}{3}}.$$

Nucleons on the surface of the nucleus are surrounded by less particles than the ones inside. They are effectively less attracted by other nucleons. The reduction of the binding energy is proportional to the surface area of the volume and the radius is proportional to the third root of the number of nucleons  $A$ .

3. The Coulomb term:

$$E_{\text{Coul}} = -a_{\text{Coul}} \cdot A^{-\frac{1}{3}} \cdot Z^2 \approx -0.67 \text{ MeV} \cdot A^{-\frac{1}{3}} \cdot Z^2.$$

The electrostatic repulsion of the positively charged protons is taken into consideration by this term. The Coulomb energy is inversely proportional to the radius of a sphere and proportional to the square of the nuclear charge  $Z$ .

4. The asymmetry term:

$$E_{\text{Asym}} = -a_{\text{Asym}} \cdot \frac{(N - Z)^2}{4A} \approx -92.86 \text{ MeV} \cdot \frac{(N - Z)^2}{4A}.$$

Empirical data show the dependence of the binding energy on the proton neutron balance  $(N - Z)$  (in the asymmetry term,  $Z$  stands for the number of protons, not

for the nuclear charge). Asymmetrical nucleons with more neutrons than protons are less stable than symmetrical nucleons with  $N = Z$ .

5. The pairing term:

$$E_{\text{Pair}} = a_{\text{Pair}} \cdot A^{-\frac{1}{2}}.$$

This term considers that an even number of protons and neutrons results in particularly stable nucleons. In the pairing term  $E_{\text{Pair}}$ ,  $a_{\text{Pair}}$  varies between even-even cores  $a_{\text{Pair}} = 11.46$  MeV, even-odd/odd-even cores  $a_{\text{Pair}} = 0$  and odd-odd cores  $a_{\text{Pair}} = -11.46$  MeV.

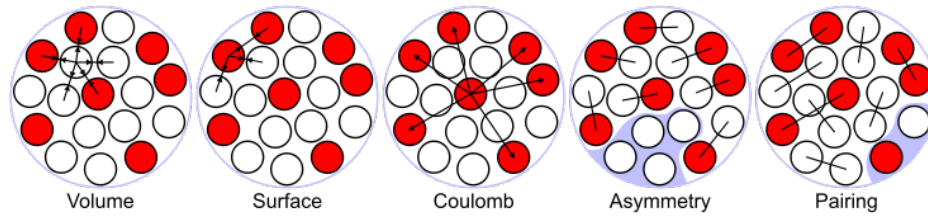


**Figure 2.4:** Illustration of the individual terms of the Bethe-Weizsäcker formula [12].

Summation of the 5 terms listed above leads to the Bethe-Weizsäcker formula, contributing to the total binding energy of a nucleus:

$$E_{\text{Tot}} = E_{\text{Cond}} + E_{\text{Sur}} + E_{\text{Coul}} + E_{\text{Asym}} + E_{\text{Pair}}. \quad (2.1)$$

### 2.2.1 Radioactive Decay

A nuclide undergoes radioactive decay if it spontaneously transforms into another more stable nuclide by emitting radiation and decreasing its initial energy. By looking at Einstein's mass energy equivalence formula  $E = mc^2$  this refers to the fact that the sum of the masses of all fractions is smaller than the mass of the mother nuclide. The rest of the energy is preserved by the gain in binding energy.

Spontaneous radioactive decay is a statistical process. An event of decay cannot be predicted in time and cannot be influenced. The radioactive half life gives information about the statistical probability of decay.

Looking at the Bethe-Weizsäcker formula (2.1) it shows that there exists a ground state for each nuclide with a constant number of nucleons, called isobar. Nuclides always tend to transform until minimum energy is reached.

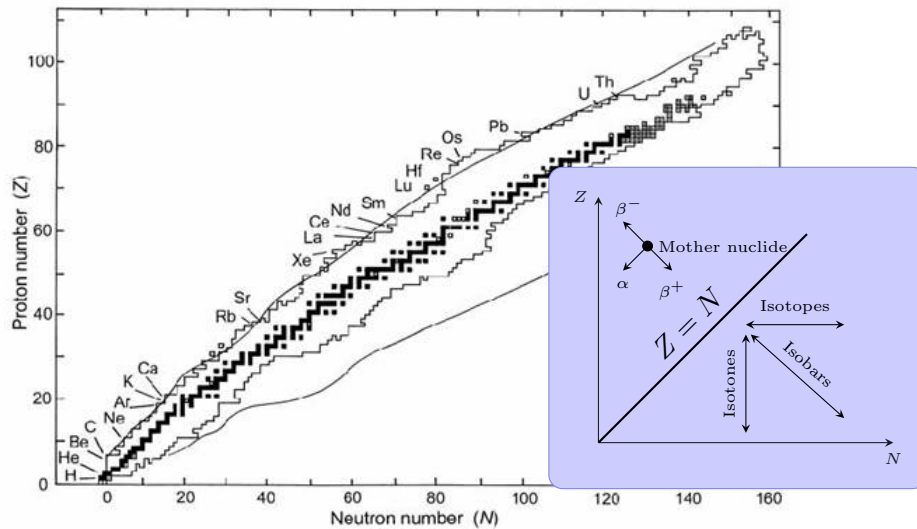


**Figure 2.5:**  $N$ - $Z$  diagram. The arrows in the right diagram represent the different decay forms. Nuclides above the continuous line have a proton excess. Nuclides below the continuous line have a neutron excess. These nuclides tend to transform to more stable cores [Figure: Courtesy of A.Hirtl].

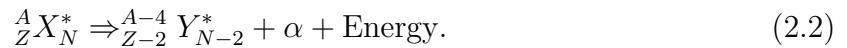
Figure 2.5 shows the influence of the number of neutrons  $N$  and protons  $Z$  on the stability of a core. The continuous line represents the stability valley, referring to nuclides with a balanced number of neutrons and protons. In practice, cores with a large number of protons tend to have a disproportionate high number of neutrons. The additional neutrons are needed to compensate the Coulomb repulsion between the protons. For heavy nuclides, the shift of the stability valley towards a higher number of neutrons compared to protons can be seen.

The arrows in figure 2.5 show possible decay channels for nuclides deviating from the line of stability: The  $\beta^-$  decay, the  $\beta^+$  decay and the electron capture. These can either happen to nuclides with a neutron excess ( $\beta^-$  decay) or to nuclides with a proton excess ( $\beta^+$  decay, electron capture). In all of these processes the number of nucleons inside the core is conserved. The third arrow in figure 2.5 parallel to the stability valley stands for the  $\alpha$  decay where an  $\alpha$  particle, consisting of 2 neutrons and 2 protons, is emitted from the nucleus. In this process the number of nucleons within the core changes.

Besides the mentioned channels of radioactive decay there exist other important decay forms. Spontaneous fission of an oscillating nucleus by splitting into two parts, inner conversion and  $\gamma$  decay. The last two decay forms have the same origin. Whilst the energy in the process of inner conversion is passed on to a shell electron leaving the atom, the energy of a  $\gamma$  decay is transported by an emitted gamma quantum. In the following section the  $\alpha$ ,  $\beta$  and  $\gamma$  decay are explained in more detail.

### 2.2.1.1 The $\alpha$ decay

When  $\alpha$  decay takes place an  $\alpha$  particle is emitted from the mother nucleus. As explained in the previous chapter an  $\alpha$  particle consists of 2 neutrons and 2 electrons, a double ionised  ${}^4\text{He}$  atom. The mass number  $A$  of the initial core is reduced by 4:



$X^*$  stands for an initial excited nucleus whilst  $Y^*$  indicates a new, possibly excited element, due to the loss of an  $\alpha$  particle.

Since only hadrons participate in this decay form, the strong force is responsible for the  $\alpha$  decay. The quantum theoretical probability for an  $\alpha$  particle leaving the nucleus depends on its binding energy in the field of Coulomb force and strong force. In classical physics this process would be prevented, quantum theoretically the  $\alpha$  particle can tunnel through the potential barrier with a certain probability. A higher energy state of the stationary  $\alpha$  particle leads to an increased probability for the particle to tunnel through the barrier (see figure 2.6). An  $\alpha$  decay from one mother nuclide in its ground state to a daughter nuclide in its ground state can also take place if the mother nuclide has a higher mass than the daughter nuclide and its  $\alpha$  particle. This difference in energy is referred to as the  $Q$  value (see equation (2.3)). Therefore  $Q$  has to be greater or equal to zero. In nature this does not occur until turning to mass numbers around 150.

$$Q = [m(Z, N, A) - m(Z - 2, N - 2, A - 4) - m({}^4\text{He})] \cdot c^2 \quad (2.3)$$

The  $\alpha$  decay energy spectrum is discrete since only one particle from a defined energy state is emitted. Decay energies typically vary from  $Q = 4 - 9$  MeV. Not all of the energy is carried by the  $\alpha$  particle due to a repulsion of the daughter nucleus.

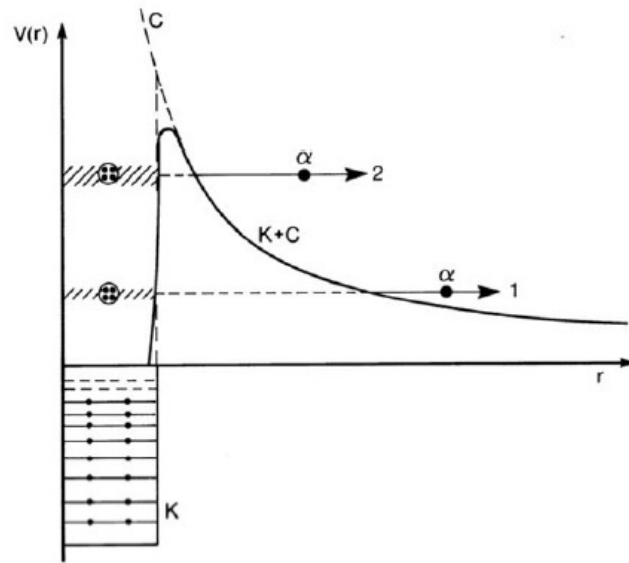


**Figure 2.6:** The energetic structure of a nucleus emitting an  $\alpha$  particle. When forming an  $\alpha$  cluster positive energy states can be enhanced due to the gain in binding energy. The  $\alpha$  particle then can tunnel through the potential barrier with a certain probability [11].

### 2.2.1.2 The $\beta$ decay

If a nuclide has an isobar neighbour in a lower energy state, most likely  $\beta$  decay is going to take place. Thereby, nucleons of the mother nuclide transform under the emission of leptonic particles. The  $\beta^-$  decay (see equation (2.4)) describes a neutron that is transformed into a proton and an electron. Due to the conservation of leptonic particles, another particle, an electron anti-neutrino is created.

In  $\beta^+$  decay (see equation (2.5)), a proton is transformed into a neutron and a positron together with an electron neutrino.

The weak force is responsible for these decay processes since leptonic particles are generated. The hadron, subjected to the strong force, remains in the core whilst the leptons, not influenced by the strong force, leave the nucleus.

$$\beta^- : \quad n \Rightarrow p + e^- + \bar{\nu} + \text{energy} \quad (2.4)$$

$$\beta^+ : \quad p \Rightarrow n + e^+ + \nu + \text{energy} \quad (2.5)$$

Regarding the Bethe-Weizsäcker formula (2.1) for isobars, the binding energy is proportional to  $A^2$ ,  $A$  standing for the number of nucleons. The energy parabolas for the corresponding isobars are shown in figure 2.7. There exists a state of minimum energy for each isobar. Both odd/even and even/odd nuclides lead to the same parabola as their pairing term in formula (2.1) equals to zero. For these isobars only one stable nuclide exists. Unstable isobars experience  $\beta^-$  or  $\beta^+$  decay to reach the ground state in the stability valley depending on whether they have to increase or decrease their number of protons. In comparison to that, nuclides with an odd/odd or even/even number of protons and neutrons are located on different parabolas due to an energy gap resulting from the pairing term. As previously explained, the pairing term for even/even nuclides results in an increased binding energy whilst it leads to a decrease in binding energy for odd/odd nuclides. The odd/odd nuclide in the lowest energy state can still decay into two even/even nuclides. It can either undergo  $\beta^-$  or  $\beta^+$  decay resulting in two different stable isobars. This can be seen in figure 2.7.

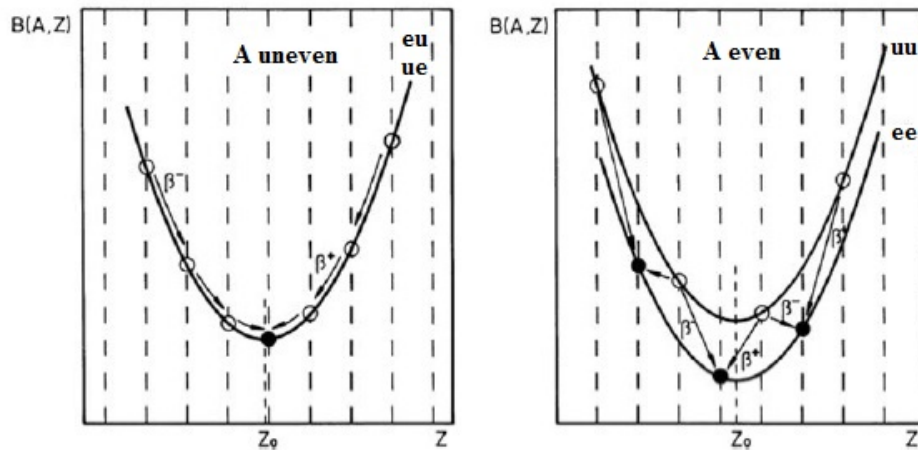


**Figure 2.7:** Energy parabolas for a nuclide with an uneven (left picture) and even (right picture) mass number  $A$ , resulting from the Bethe Weizsäcker formula [11].

At the beginning of the 20th century it was experimentally shown that the energy distribution of electrons emitted by a  $\beta^-$  decaying nucleus is continuous. The kinetic energy gained through  $\beta$  decay is split amongst the  $\beta$  particle, the (anti-)neutrino and the daughter nuclide. The statistic kinetic energy distribution for the  $\beta$  particle and the (anti-)neutrino results in a  $\beta$  particle with a possible kinetic energy from zero to the maximum available energy. A correction concerning the Coulomb interaction between the daughter nuclide

and the  $\beta$  particle leads to slightly shifted curves (figure 2.8). The negatively charged electrons are attracted by the nucleus. To overcome the Coulomb barrier an amount of energy is needed. Therefore the  $\beta^-$  distribution is shifted towards lower energies. In contrast to this, the positively charged positrons are repelled by the nucleus, leading to a shift in the  $\beta^+$  distribution towards higher energies.

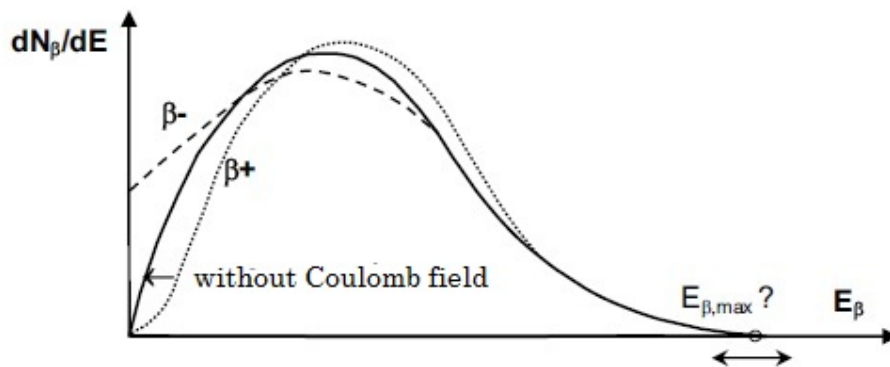


**Figure 2.8:** Kinetic energy distribution of  $\beta$  particles. The  $\beta$  decay represented by the continuous line does not include the Coulomb force. This force is considered by the spectra of the dotted ( $\beta^+$ ) and dashed ( $\beta^-$ ) lines [11].

**Positron Annihilation** Since a particle can annihilate with its anti-particle, a positron can annihilate with an electron (the positron is the anti-particle of an electron). Regarding mass and energy equivalence, two  $\gamma$  rays are emitted in an annihilation process. The energy of these two  $\gamma$  rays is 511 keV each and corresponds to the rest energies of the electron and the positron. If these two particles are at rest at the moment of annihilation the  $\gamma$  rays are emitted in anti-parallel directions, contributing to the conservation of momentum.  $\gamma$  rays originating from particles not completely at rest are emitted with an angle slightly smaller than  $180^\circ$ . This circumstance, called non-collinearity, is an important limiting factor in PET image resolution (see section 2.3.5).

Positron annihilation can also take place in the opposite direction when a photon with an energy higher or equal to the sum of the rest energies of a positron and an electron (1022 keV) generates these particles. This process is called pair production and is described in more detail in section 2.2.3.

Positron annihilation is fundamental for the functionality of PET imaging.

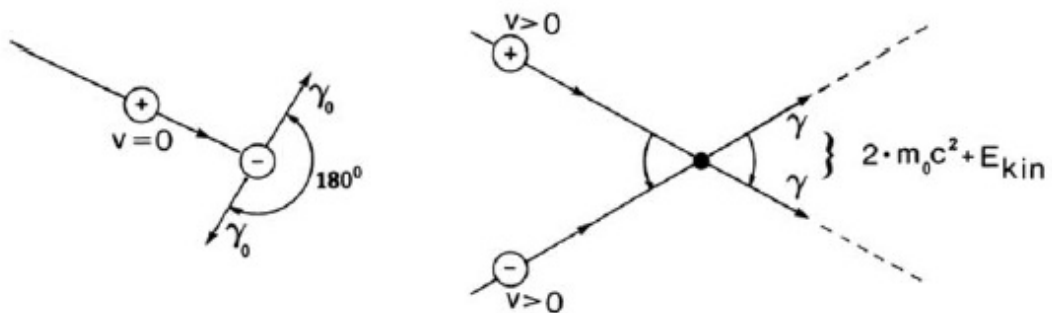


**Figure 2.9:** Positron annihilation. Left: At the annihilation point, positron and electron are at rest. Right:  $v \neq 0$  for positron and electron. The preservation of momentum causes a deviation of the  $180^\circ$  angle between the two photons [11].

### 2.2.1.3 The $\gamma$ Decay

The transformation of a core to a less excited state of energy can also go along with  $\gamma$  decay. In this form of radioactive decay no particles are emitted from the nucleus but a highly energetic  $\gamma$  quantum. This can happen if the energy excess of the mother nuclide is too small for particle emission. Like electrons in the shell of an atom, nucleons can be in an excited state as well. Since  $\gamma$  rays are of electromagnetic nature the mass number of the nuclide does not change. The released energy is expressed by the lower mass of the daughter nuclide. With respect to Einstein's energy mass equivalence this corresponds to a state of lower energy and higher stability. Usually,  $\gamma$  rays are defined as electromagnetic waves with energies higher than 200 keV.

## 2.2.2 Nuclide Production

Radioactive nuclide production is a main task in nuclear medicine since most of the nuclides have a low natural appearance. The basic principle is to create unstable cores by weakening the binding energy of an original nuclide.

One method is called neutron activation: A target atom gets bombarded with neutrons that can be taken up by the atom. This leads to a  $\beta^-$  emitter whilst proton bombardment leads primarily to  $\beta^+$  emitters. The deranged neutron-proton ratio results in unstable activated cores.

An example for this is the nuclide production of Fluorine 18 ( $^{18}\text{F}$ ), commonly used in

PET imaging. It is created by proton bombardment of an Oxygen 18 ( $^{18}\text{O}$ ) target. The nucleus takes up a proton and emits a neutron. The reaction equation can be seen below:



$^{90}\text{Y}$  used in SIRT is produced in a high-purity separation from its mother nuclide Strontium 90 ( $^{90}\text{Sr}$ ).  $^{90}\text{Sr}$  itself is a fission product of uranium in nuclear reactors. Figure 2.10 shows the decay scheme of  $^{90}\text{Y}$ . The  $0^+ \rightarrow 0^+$   $^{90}\text{Zr}$  transition is responsible for the occurrence of inner pair production.

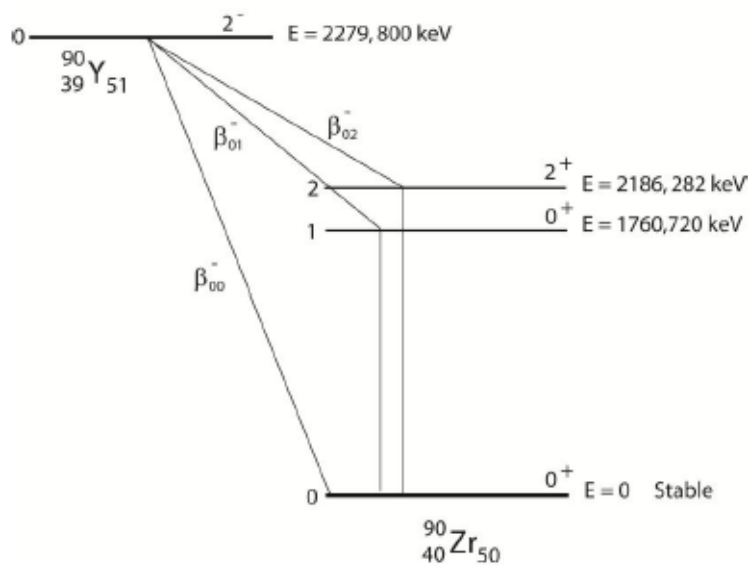


Figure 2.10: Decay scheme of  $^{90}\text{Y}$  [1].

### 2.2.3 Photon Interaction with Matter

There exist 5 major forms of interaction of radiation with matter. A photon can interact with the shell of an atom as well as with the Coulomb field of the nucleus. This includes absorption and scattering of the initial photon. Whilst the first 3 processes described in this chapter (coherent scattering, Compton scattering and photoelectric effect) depict interactions with the atomic shell, pair production and nuclear photo reaction occur in the field of the nucleus (nuclear photo reaction is not important in PET imaging since energies of several MeV are required). The sum of these 5 forms leads to the attenuation

coefficient  $\mu$  of a certain material.

**Coherent Scattering** In this process, which is also called Thomson scattering or, within the range of visible light, Rayleigh scattering, the photon is scattered in the field of the atomic shell without energy loss. The atomic shell therefore remains unchanged. In fact, the initial photon induces the atomic shell to oscillate with the same frequency as the incoming photon. The coherent oscillating shell acts like a transmitter and transfers the energy back to the photon. This can be seen in figure 2.11.

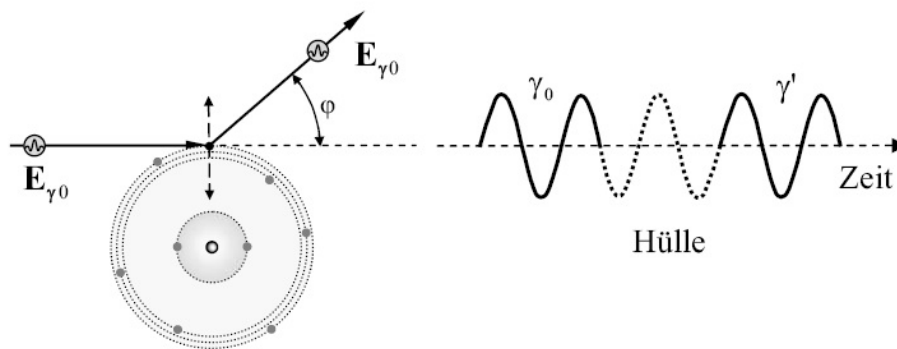


**Figure 2.11:** Coherent Scattering. Left: The photon is scattered at an atomic shell's electron. The direction of photon propagation changes, the electron remains in the atom. Right: Phase correlation between the incoming photon, oscillation of the electronic shell and the scattered photon [11].

Coherent scattering broadens the initial beam but does not diminish its energy. No energy is taken up by the absorber. The occurrence of this process is proportional to the density of the absorber material  $\rho$ . This, together with the dependence on the photon energy  $E_\gamma$  and the atomic number  $Z$ , leads to the overall coherent scattering coefficient  $\sigma_{Cl}$  for energies higher than 10 keV:

$$\sigma_{Cl} \propto \rho \cdot \frac{Z^{1.5}}{E_\gamma^2}. \quad (2.7)$$

Coherent scattering for low atomic numbers like in human tissue or water is therefore just relevant for photon energies below 20 keV.

**Compton Scattering** This is the inelastic form of coherent scattering. A photon interacts with a loosely bound outer shell electron, transmits some of its energy and momentum

and the electron leaves the atom. This leads to a reduced photon energy and therefore a larger wavelength.

The two body interaction can be treated like classical scattering by reason of the wave particle duality. With the conservation of energy and momentum one can derive the energy transferred from the photon to the electron. Regarding an electron at rest this leads to the energy of the scattered photon:

$$E'_\gamma = \frac{E_\gamma}{1 + \frac{E_\gamma}{m_0 \cdot c^2} \cdot (1 - \cos(\varphi))}. \quad (2.8)$$

The energy of the Compton scattered electron is the difference between the initial and scattered photon energy together with the binding energy of the electron. Since the electron is estimated to be bound loosely to the atom this term can be neglected:

$$E_{\text{kin}} = E_\gamma - E'_\gamma - E_b \approx E_\gamma - E'_\gamma. \quad (2.9)$$

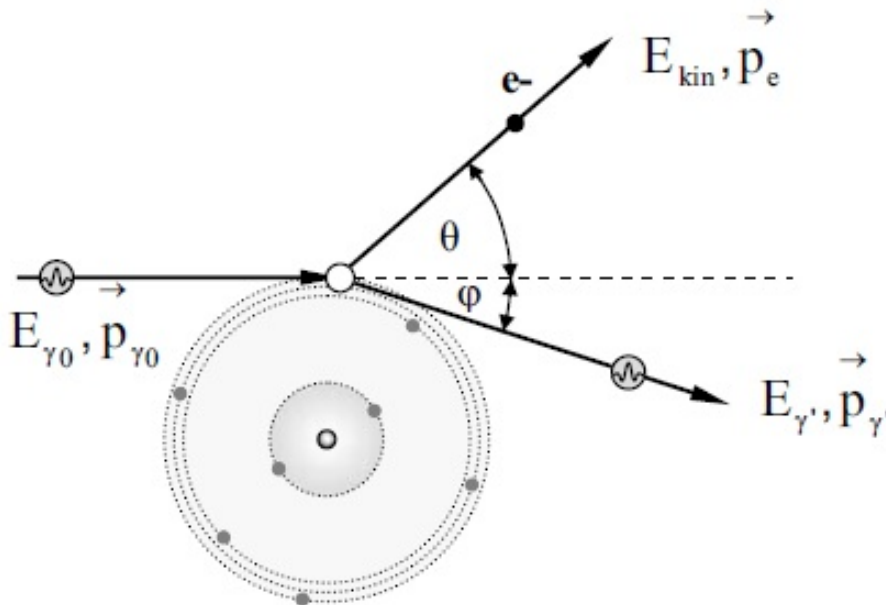


**Figure 2.12:** Compton effect: Photon scattering with an outer shell electron. The electron leaves the atom and the photon energy and direction changes [11].

The probability of Compton scattering is represented by the Compton interaction coefficient  $\sigma_C$ . Because two particles appear in a Compton scattering process, the interaction

coefficient  $\sigma_C$  is the sum of  $\sigma_{\text{scatt}}$  and  $\sigma_{\text{tr}}$ , where  $\sigma_{\text{scatt}}$  stands for the incoherent photon scattering and  $\sigma_{\text{tr}}$  covers the energy transfer from the photon to the Compton electron. Quantum physical analysis show that the probability of Compton scattering is proportional to the ratio between the atomic number and the mass number of the absorber atom  $Z/A$ . For most of the stable and light elements  $Z/A \approx \frac{1}{2}$  and therefore the Compton scattering coefficient is widely independent from the atomic number. Like other photon interaction coefficients, Compton scattering is also proportional to the density  $\rho$  of the absorber material. There exist no simple relation for the energy dependence of the Compton coefficient. Equation (2.10) shows an approximation for the Compton coefficient energy dependence in the photon energy range from 0.2 – 10 MeV where Compton scattering is dominant.

$$\sigma_C \propto \rho \cdot \frac{Z}{A} \cdot \frac{1}{E_\gamma^n} \quad (n = 0.5 - 1) \quad (2.10)$$

**Photoelectric Effect** A photon gets absorbed by an inner shell electron. With the gained energy, the electron is able to leave the atom with a kinetic energy equal to the photon energy minus the binding energy of the electron:

$$E_{\text{kin}} = E_\gamma - E_B. \quad (2.11)$$

Therefore, the photoelectric effect can only take place if the photon energy is higher than the binding energy of the electron. For reasons of conservation of momentum a small amount of energy is also transferred to the atom. Due to its high mass compared to the electron this energy transfer can be neglected. The absent electron is replaced by an outer shell electron reducing its energy by emitting characteristic  $\gamma$  rays.

The probability of this effect is given by the photo absorption coefficient  $\tau$ . It depends on the material density  $\rho$  and is proportional to the inner shell electronic density which is proportional to  $Z^3$ . More detailed theoretical and numerical examinations lead to the following dependence of  $\tau$  on the atomic number  $Z$ :

$$\tau \propto \rho \cdot \frac{Z^n}{A} \approx \rho \cdot \frac{Z^{4-4.5}}{A}. \quad (2.12)$$

For low atomic numbers the exponent  $n$  of  $Z$  is approximately 4.5 and for heavier atoms  $n$  is about 4.

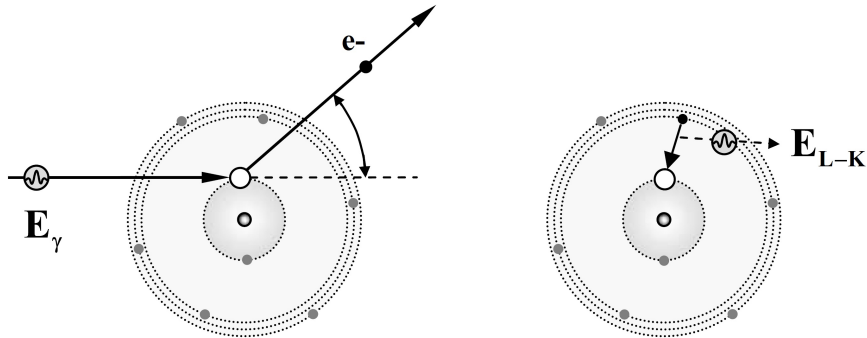


**Figure 2.13:** Photoelectric effect: The photon is absorbed by transferring its energy to an inner shell electron which leaves the atom. The hole is filled by an outer shell electron under the emission of characteristic x-rays [11].

**Pair Production** Photons can also interact in the electric field of charged particles like atomic nuclei or electrons. When the photon energy exceeds the energy mass equivalence for two electrons ( $2 \cdot 511$  keV), an electron positron pair can be formed in strong Coulomb fields. The energy of the photon is transformed partly into the rest masses of the particles as well as into their kinetic energies (see equation (2.13)). The photon is completely absorbed in this process (see figure 2.14).

$$E_{\text{kin}} = E_\gamma - 2 \cdot m_0 \cdot c^2 = E_\gamma - 1022 \text{ keV} \quad (2.13)$$

In equation (2.13),  $m_0$  stands for the rest mass of the electron and positron. It can be seen that pair production is only possible for photon energies higher than 1022 keV and does not occur at lower energies. The kinetic energy  $E_{\text{kin}}$  is split up between the electron and the positron. Since the positron has got a positive charge and is rejected by the atomic nucleus its kinetic energy, in general, is slightly higher than the kinetic energy of the electron that gets attracted by the nucleus.

At high energies this process can also take place in the Coulomb field of an electron. Since the mass of an electron is much smaller than the mass of a nucleus, the electron can leave the atom by reason of the transferred momentum. Due to the fact that three particles are emitted this process is called triplet production, with the corresponding interaction coefficient  $\kappa_{\text{Tripl}}$ .

The probability of pair production is proportional to the logarithm of the photon energy

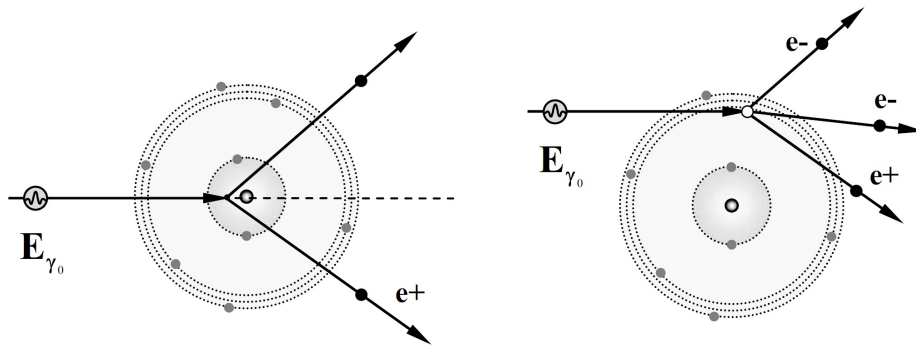


**Figure 2.14:** Pair production. Left: Schematic picture of pair production in the Coulomb field of a nucleus. The created electron positron pair is emitted in the direction of photon propagation because of momentum conservation. Right: Triplet Production in the Coulomb field of an electron [11].

and the ratio  $Z^2/A$  between the atomic number  $Z$  and the mass number  $A$ . For most light elements this leads to an energy and atomic number dependence as follows:

$$\kappa_{\text{Pair}} \propto Z \cdot \rho \cdot \log(E_\gamma). \quad (2.14)$$

The reverse process occurs when the positron loses its energy through interactions with the absorber material, comes to rest and recombines with an electron by sending out two 511 keV photons (see section 2.2.1.2).

## 2.2.4 Attenuation of Photons

In the previous chapter the different forms of photon interactions with matter were described. The sum of the probability coefficients for each of these processes leads to the linear attenuation coefficient  $\mu$  which is an important characteristic for an absorber material:

$$\mu = \tau + \sigma_C + \sigma_{\text{Cl}} + \kappa_{\text{Pair}} + \kappa_{\text{Tripl}}. \quad (2.15)$$

Since photons carry no charge they have quite low interaction probabilities in a certain absorber material. The description of these probabilities can be found in the attenuation law. It is credible for large numbers of particles but not for individual particles because of statistical fluctuations.

The transmission  $T(x)$  is the ratio between the number of photons  $N(x)$  behind an absorber with thickness  $x$  and the number of initial photons  $N$ :

$$T(x) = \frac{N(x)}{N}. \quad (2.16)$$

If the changing number of initial particles  $dN$  is proportional to the number of particles  $N$  at the beginning, the decrease of particles can be written as follows in the differential form of the law of attenuation (equation (2.17)) where narrow beam geometry and mono energetic photons are assumed:

$$dN = -\mu \cdot N \cdot dx. \quad (2.17)$$

The common way of illustrating the law of attenuation is found in its integral form:

$$N(x) = N \cdot e^{-\mu \cdot x}. \quad (2.18)$$

The law of attenuation does not apply to non-monoenergetic photons because of the energy dependent attenuation coefficient of uncharged particles. This can lead to beam hardening, well known in several processes of radiation physics. High energetic photons are being attenuated less than low energetic photons. The shift to higher energetic photons results in a smaller linear attenuation coefficient.

Since the linear attenuation coefficient  $\mu$  varies with the absorber density the mass attenuation coefficient  $\mu_m$  can be used. It represents the linear attenuation coefficient divided by the density of the absorber.

## 2.3 PET/CT - Positron Emission Tomography/Computed Tomography

Positron Emission Tomography (PET) is a highly sensitive imaging technique in modern nuclear medicine. Nowadays many PET systems are combined with Computer Tomography (CT), resulting in an interaction of their individual advantages. Whilst PET provides information on the human metabolism, CT results in a good spatial resolution. Besides that, CT gives the possibility to measure human tissue densities and perform attenuation correction (see section 2.3.6) which is important for PET imaging.

### 2.3.1 Basic Functionality

Even though there exist several types of PET systems, all of them are based on the same principles. A certain radioactive substance providing positrons is injected into the human body.  $^{18}\text{F}$ , for example, is a commonly used  $\beta^+$  emitter for PET imaging. In PET, 511 keV photons originating from an annihilation process between a positron and an electron from the absorber object are detected. A signal is formed when two  $\gamma$  rays are detected within a predefined coincidence window.

Similar to the gamma camera, the scintillating crystal transforms the 511 keV photons into visible light resulting in a higher detection efficiency. The photons then reach the photomultiplier tubes where the signal is amplified.

### 2.3.2 Scanner Design

Divers scanner geometries are used to acquire  $360^\circ$  data sampling as it is necessary for the detection of isotropic annihilation photons. The most common type is the full ring circular PET with crystals arranged along a full circle. Another type is the partial ring circular system with continuous rotation to provide  $360^\circ$  data sampling. Some devices also use a flat detector design. An illustration of the mentioned scanner types can be found in figure 2.15.

### 2.3.3 Detectors

Most of the modern PET scanners use detectors based on the block design by Casey and Nutt [14]. It consists of a main block of scintillating material and photomultiplier tubes. Common scintillating materials used are bismuth germanate (BGO) and lutetium oxyorthosilicate (LSO). Major factors for choosing a scintillator are the stopping power dependent on the density, the brightness (number of light photons produced per 511 keV interaction), the wavelength of the emitted light or the time needed to produce the light. In this diploma thesis LSO crystals were simulated.

The main scintillating block (typically  $4 \times 4$  cm with a depth of 3 cm) is segmented into an array of smaller parts (typically  $8 \times 8$ ). These parts are surrounded by an optical reflective material to isolate the individual elements within the block. The depth of the segmentation is dependent on the location of the block element (see figure 2.16). In the block corner the cut filled with reflective material is deeper than in the middle of the block.

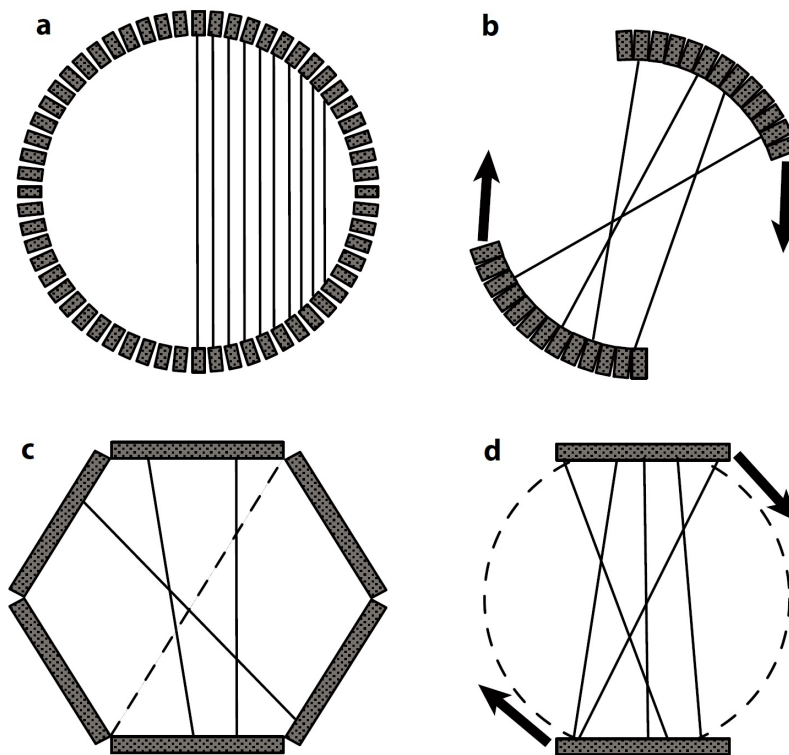


**Figure 2.15:** Different PET detector types: a) non-rotating full ring circular system, b) partial ring circular system with continuous rotation, c) non-rotating ring with flat detectors, d) gamma camera PET (two gamma cameras are used as a PET detector). The continuous lines in the pictures represent possible lines of response (LORs) [13].

Scintillation light coming from the corner should be transmitted to the photomultiplier right behind it whilst signals originating from the center should be spread roughly equal amongst the photomultiplier tubes. Photomultiplier tubes, as they are frequently used in several technical applications, form an amplified electrical signal out of the scintillation light.

### 2.3.4 Types of Coincidences

There are 4 types of coincidences that occur and are detected by a PET system: True, scattered, random and multiple coincidences. A description and a schematic picture (see figure 2.17) of these 4 types of coincidences can be found below.

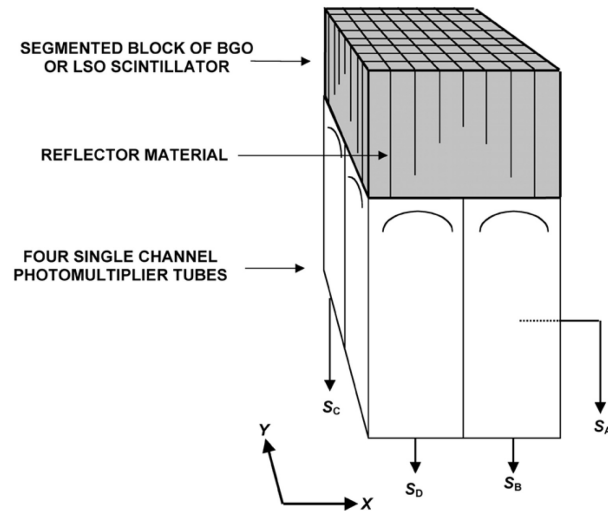


**Figure 2.16:** Visualization of the block detector design. The segmented block of scintillating crystal is followed by an array of photomultiplier tubes [15].

**True Coincidences** Detection of a photon pair originating from one electron positron annihilation. An ideal true coincidence refers to two unscattered photons.

**Scattered Coincidences** At least one of the two photons originating from one event of annihilation gets scattered on the way to the detector. Scattering leads to a shift in the line of response (LOR) and causes the involved photon to lose some of its initial energy.

**Random Coincidences** Two photons emanating from different electron positron annihilations detected within a certain time window lead to a random coincidence.

**Multiple Coincidences** This event is closely related to random coincidences. Multiples occur when more than two photons are detected in coincidence.

Only true coincidences account for the real activity distribution of the radioactive source. All the other types of coincidences lead to noise in the reconstructed image because of a false LOR.

The acceptance of a pair of photons in coincidence is controlled by a system dependent time window, the so called coincidence window. Only photons detected within this time are interpreted as true coincidences. A predefined energy window is used to take photons into account that have not or just slightly been scattered on their way to the detector

crystal. Photons that have gone through more intense scattering processes and therefore have lost a certain amount of energy are cut off by the energy filter.

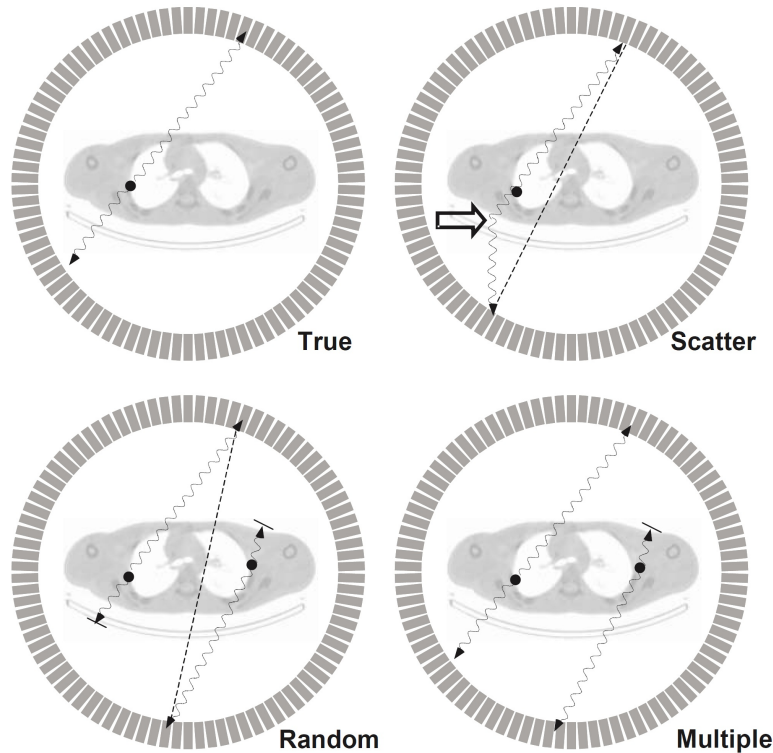


**Figure 2.17:** Different types of coincidences. True (upper left), scattered (upper right), random (lower left) and multiple coincidence (lower right) [13].

### 2.3.5 Spatial Resolution

Spatial resolution in a PET system depends on two factors, the positron range and the non-collinearity (see figure 2.18).

The positron range depicts the distance between the place of origin of the positron and the point of electron positron annihilation. Though one is interested in the place of radioactive decay, the PET system can just detect the annihilation point with the corresponding LOR. The extent of the positron range is energy dependent and therefore radionuclide dependent since different nuclides have different  $\beta$  energies.

Annihilation of an electron positron pair perfectly at rest leads to two anti-parallel ( $180^\circ$ ) emitted photons due to the conservation of momentum. Non-collinearity takes into account

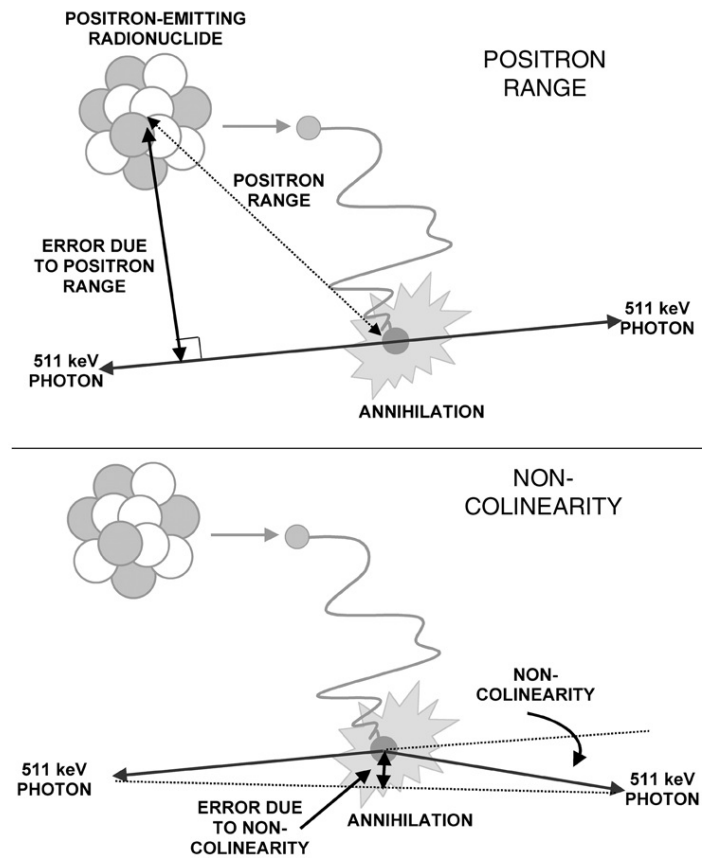


**Figure 2.18:** Limiting factors for the spatial resolution: Positron range (upper picture) and non-collinearity (lower picture) [15].

that the electron and the positron are not completely at rest at the time of annihilation. This leads to two photons propagating with an angle slightly deviating from  $180^\circ$ . This effect is not energy dependent.

Besides the resolution limit reachable due to the physical properties of the positron decay, the detector design as well as the system geometry also account for the final resolution. The intrinsic detector resolution depends on two main components of geometric and physical nature.

The geometric component describes the best reachable resolution when regarding a detection material with 100% detection efficiency.

The physical component includes all the non-ideal properties of the detector resulting in a detection efficiency lower than 100%. A visualisation of the geometric resolution com-

ponent can be seen in figure 2.19. The full width at half maximum (FWHM) in the center of the field of view (FOV) equals one half of the detector width  $w$  and increases linearly moving the source towards one detector where the FWHM is approximately equal to the detector width  $w$ .

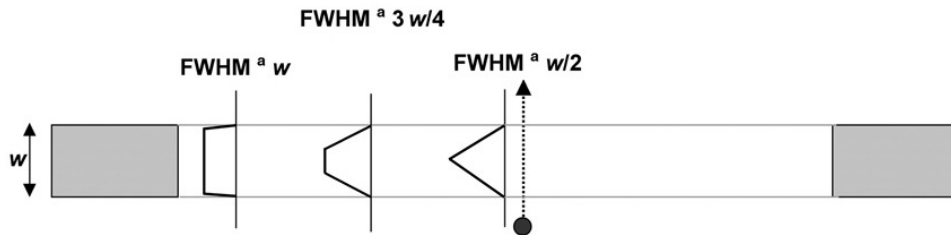


**Figure 2.19:** Geometric spatial resolution dependent on the location of a point source between two detectors of widths  $w$ . The FWHM increases linearly when moving the point source from the center towards one of the two detectors [15].

The thickness of the scintillating crystals leads to another geometric effect called detector parallax. It considers the fact that annihilation photons can interact at any depth inside the scintillating crystal. Whilst a photon at the center of the FOV enters the crystal perpendicular to its surface, this is not the case for photons with a radial offset. These photons may penetrate the first crystal and be detected in the crystal next to the first one. The two consequences of this effect are a broadening of the response function due to a larger area of the LOR and a false location of the event towards the center of the scanner (see figure 2.20).

### 2.3.6 Attenuation Correction

Attenuation of a 511 keV annihilation photon in a certain LOR takes place when it is absorbed or scattered into another LOR. This means the annihilation event is not just referred to the wrong LOR, but also removed from the true LOR.

As explained in section 2.2.4, photons follow an exponential attenuation law. The single photon count rate  $C$  after travelling through an attenuating medium with depth  $a$  and linear attenuation coefficient  $\mu$  is

$$C = C_0 \cdot e^{-\mu a}. \quad (2.19)$$

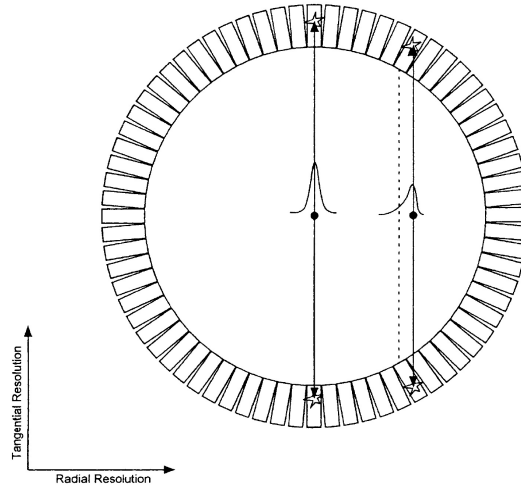


**Figure 2.20:** Detector parallax: The response function gets asymmetrical with an increasing radial offset due to detector penetration and an unknown interaction depth [15].

Considering the case of PET where two photons in coincidence are detected, the count rate for detecting both photons is given by the product of the individual photon count probabilities. These photons are emitted anti-parallel, leading to the following equation:

$$C = C_0 \cdot e^{-\mu a} \cdot C_0 \cdot e^{-\mu(D-a)} = C_0 \cdot e^{-\mu D}. \quad (2.20)$$

In equation (2.20),  $D$  stands for the overall thickness of the tissue in a certain LOR. It can be seen that attenuation is just dependent on the total thickness but not on the source depth along this LOR.

Attenuation correction is done by performing a LOR dependent blank scan  $B(\text{LOR})$  without the patient, and a LOR dependent transmission scan  $T(\text{LOR})$ . The attenuation correction factor  $ACF$  for each LOR is then given by:

$$ACF(\text{LOR}) = \frac{B(\text{LOR})}{T(\text{LOR})}. \quad (2.21)$$

### 2.3.7 Data Representation - Sinogram

The raw data of the detected annihilation photons gathered by a PET scanner is usually depicted in a 2-D matrix  $S(s, \Phi)$  which is called sinogram. The elements of this matrix include all the events referring to different LORs, therefore to different detector pairs.

The correlation between LORs and a sinogram is presented in figure 2.21.

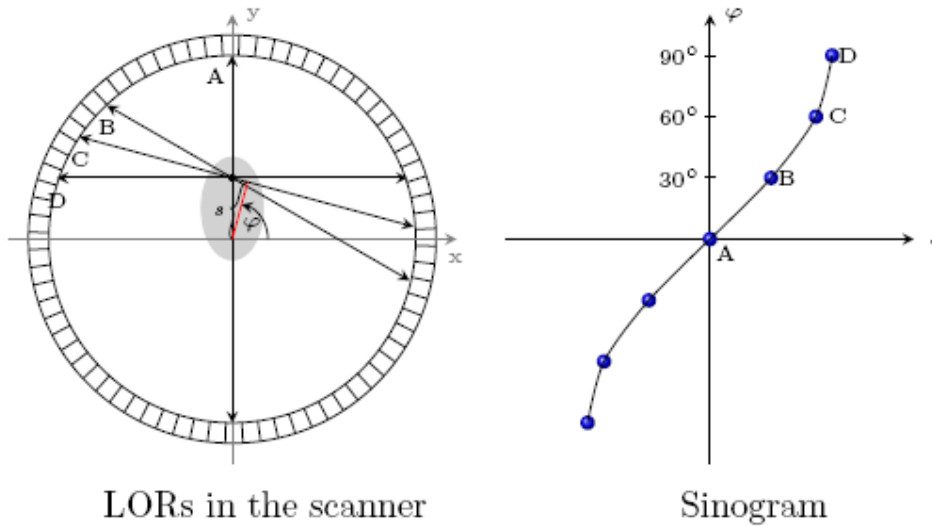


**Figure 2.21:** Correlation between different lines of response (LORs) inside the scanner and its sinogram, defined by the coordinates  $s$  and  $\Phi$  [Figure: Courtesy of A. Hirtl].

A sinogram matrix is characterized by its coordinates  $s$  and  $\Phi$ , where each row represents a projection ( $\Phi$  is constant) and each column represents a fixed radial offset  $s$  from the center of the scanner. The relation between the sinogram coordinates  $(s, \Phi)$  and the object space coordinates  $(x, y)$  is given by equation (2.22).

$$s = x\cos\Phi + y\sin\Phi \quad (2.22)$$

## 2.4 Image Reconstruction

An important task in medical imaging is the 3D reconstruction of a measured object out of the gained raw data.

There are two basic approaches of algorithms for image reconstruction. The first form tries to generate an image with analytic mathematical reconstruction methods. The other method iteratively reconstructs an appropriate image out of a data collection set using reasonable criteria.

### 2.4.1 Filtered Back Projection

Filtered back projection (FBP) is based on the mathematical correlation between an object function  $f(x, y)$  and its measured projections  $P_\theta(t)$  along the corresponding line element  $ds$ , called the radon transform:

$$P_\theta(t) = \int_{\text{line}(t,\theta)} f(x, y) ds = \int_{-\infty}^{\infty} \int_{-\infty}^{\infty} f(x, y) \delta(x \cos \theta + y \sin \theta - t) dx dy. \quad (2.23)$$

The FBP is given by:

$$f(x, y) \approx \frac{\pi}{K} \sum_{i=0}^K \int_{-W}^W S_{\theta_i}(\omega) |\omega| e^{2\pi i \omega t_i} d\omega. \quad (2.24)$$

In equation (2.24)  $K$  stands for the number of projections,  $S_{\theta_i}$  are the Fourier transformed projections  $P_\theta(t)$  and  $|\omega|$  with its integral limits represents the ramp filter used in FBP to suppress the occurring  $1/r$  blurring. For a more detailed discussion of the given formulas the reader is referred to literature [16].

Advantages of FBP are that it works very fast and does not need a lot of data storage since each projection is only used once for image reconstruction.

FBP does not take into account the statistical nature of the imaging process and it is not possible to imply scatter or geometry corrections directly into the reconstruction process leading to image artefacts.

### 2.4.2 Iterative Reconstruction

A fundamentally different method is iterative image reconstruction. The basic idea is to compare iteratively estimated images with the measured projection data until a certain accuracy is reached.

In practice an initial guess of the activity  $a_i$  in a certain pixel  $i$  is made. To get the projection data  $s_j$  of a detector pair  $j$  out of the radioactivity distribution of the initial guess, the system matrix  $M_{i,j}$  is used:

$$s_j = \sum_{i=1}^I M_{i,j} a_i. \quad (2.25)$$

This process called forward projection is necessary to be able to compare the projection

data of the image guess with the measured projection data.

The system matrix  $M_{i,j}$  can be seen as the probability that a decay in pixel  $i$  is detected by the detector pair  $j$  and is normalized to an overall detection probability of 1 regarding  $D$  detector pairs.

$$\sum_{j=1}^D M_{i,j} = 1 \quad (2.26)$$

The aim is to iteratively correct the guess of the activity distribution  $a_i$  and repeat the explained steps until a certain abort criteria is reached.

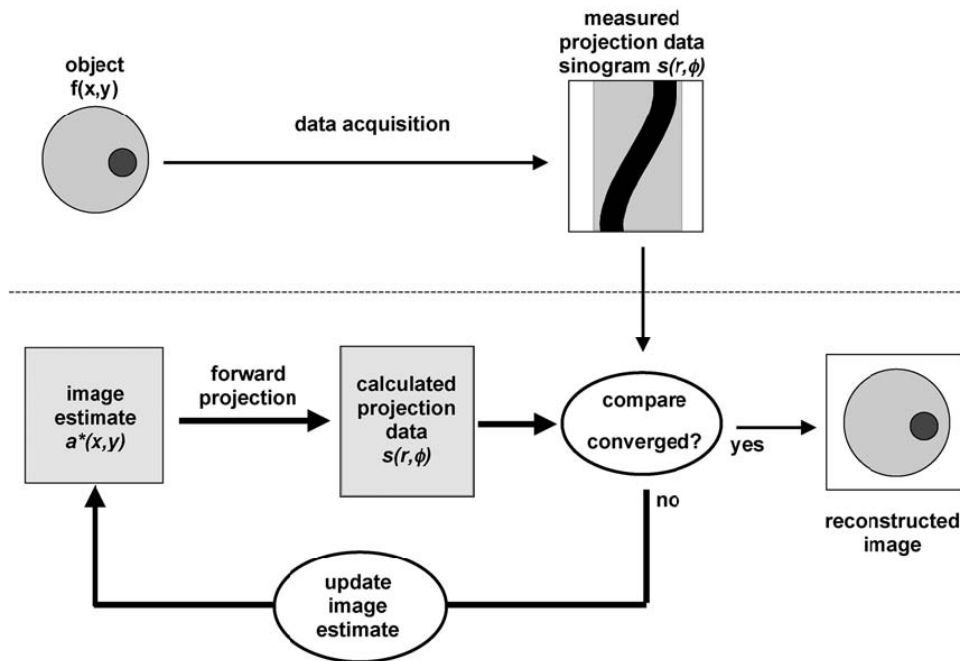


**Figure 2.22:** Basic structure of an iterative image reconstruction. An activity distribution is estimated, forward projected and compared to the measured projection data until a defined level of convergence is reached [15].

Advantages of iterative reconstruction can be found in the possible implementation of geometric or scattering effects into the system matrix.

A possible disadvantage can be found in computation time. In general, the reconstruction time is much higher than using FBP.

### 2.4.2.1 OSEM Algorithm

A commonly used iterative method is the expectation maximization (EM) algorithm. The method was developed by Shepp and Vardi in 1982 [17]. This maximum likelihood based estimation iteratively calculates a new estimate  $a_{n+1}(i)$  from an old estimate  $a_n(i)$ :

$$a_{n+1}(i) = a_n(i) \sum_{j=1}^D \frac{s(j)M(i, j)}{\sum_{i'=1}^I a_n(i')M(i', j)}. \quad (2.27)$$

In this procedure, the accordance of each new guess  $a_{n+1}(i)$  with the real activity  $a(i)$  increases with every step of iteration. A Poisson activity distribution of the measured data is assumed.

In 1994, Hudson and Larkin developed the ordered subset (OS) method [18], used to shorten the computing time for image reconstruction. The projection data  $s_j$  is split into different subsets. By correcting just one subset, a new guess  $a_{n+1}(i)$  can be made. A run through all subsets is referred to one iteration.

Using OSEM, the reduction in computing time is approximately equal to the number of subsets  $s$ . The image quality of OSEM reconstruction with  $i$  iterations and  $s$  subsets is determined by  $i \times s$ . In most applications, values of  $i \times s \geq 50$  are used.



## 3 Materials and Methods

Common software programs for the computer modelling of nuclear imaging were used in this thesis. The PET simulation of the  $^{90}\text{Y}$  source was executed with Geant 4 Application for Tomographic Emission (GATE), an open source software specialised on the simulation of nuclear imaging techniques.

Image reconstruction, on the basis of the simulation raw data, was accomplished using the program STIR (Software for Tomographic Image Reconstruction). Further programs were needed for data and image manipulation.

### 3.1 Siemens TruePoint PET/CT

To provide comparable data for prospective research and development, a PET device with similar characteristics as the device located at the MedUni Vienna (Siemens TruePoint PET/CT [19]) was modelled using GATE. Important parameters from the original data sheet used for constructing the device can be found in table 3.1. A picture of the Siemens TruePoint PET/CT at the MedUni Vienna can be found in figure 3.1.

### 3.2 Source and Phantom

For the executed simulations an adapted configuration of the standardized NEMA IEC body phantom [20] was used. It consists of 6 spherical sources surrounded by a water-filled cavity. The volumes of the sources are 0.52, 1.15, 2.57, 5.58, 11.49 and 26.50 ml where 0.52 ml corresponds to a source diameter of 1 cm. The standardized NEMA IEC phantom is a body shaped water tank, with a cylindrical styrofoam insert to simulate the attenuation of the lung. In the phantom used within this work the lung insert was neglected and the body shaped water tank was approximated by a cylindrical water tank with a diameter of 25.6 cm and a height of 18 cm.

Detector material	Lutetium Oxyorthosilicate (LSO)
Crystal dimensions	4.0 × 4.0 × 20 mm
Crystals per detector block	169
Number of detector blocks	192
Photomultiplier tubes	4 per block
Detector ring diameter	842 mm
Detectors per ring	624
Number of detector rings	52
Total number of detectors	32448
Transaxial FOV	605 mm
Axial FOV	216 mm
Number of image planes	109
Plane spacing	2 mm
Coincidence window	4.1 nsec

**Table 3.1:** Extract from the Siemens TruePoint PET/CT data sheet [19].



**Figure 3.1:** Siemens TruePoint PET/CT at the MedUni Vienna [Figure: Courtesy of A. Hirtl].

### 3.3 PET Simulation

In the field of nuclear medicine GATE is a useful method for simulating tomographic emission like PET. With this software it is possible to build up a user defined system with specific properties of the tomographic device. This includes, amongst others, PET characteristics, definition of the source and phantom and the occurrence of physical processes.

#### 3.3.1 GATE

A simulation in GATE [21] is based on the stochastic method of Monte Carlo simulation. Complex problems like the radioactive decay of a substance with a huge amount of decay events are not to be solved analytically. The aim of this statistical model is to give numerical solutions for mean values of corresponding microscopic quantities. In Monte Carlo simulation the exact solution is approximated by a summation over a randomly chosen subset.

The structure of GATE is divided into 3 levels: The core level, the application level and the user level (see figure 3.2). The core level delivers all basic information needed for the simulation. This includes the geometry of the system, the appearance of physical processes and the visualisation of the simulation.

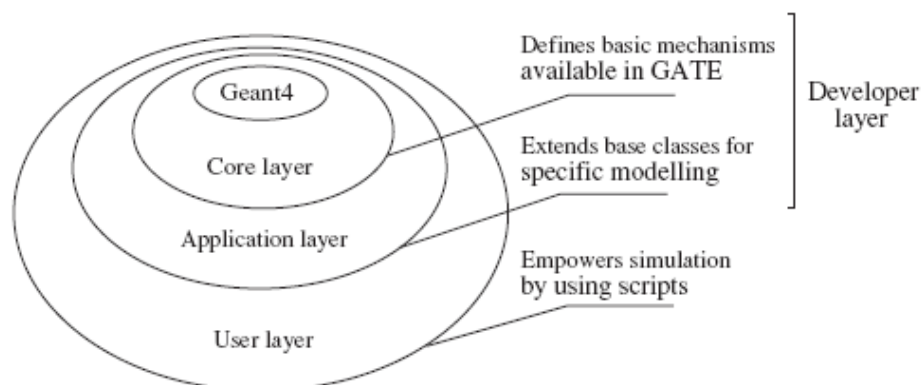


**Figure 3.2:** Structure of GATE. Simulation properties are defined in the developer layer. The user layers computational language is transformed into the GATE internal used script language C++ [21].

In the application level basic classes of the core level can be specified. For instance one

can set up the geometry of a radioactive source by defining *volume* in the core level. In the application level this definition is specified to *trapezoid*, *box*, *sphere* or other types of volumes. Movement and rotation of a predefined class are also defined within this level. The user level provides the mechanism for the script language used in GATE to correspond with the core level that uses C++. With this method the user effectively has to have no knowledge of C++ computer-oriented language.

A simulation source code written and executed with GATE together with a detailed description and visualisation can be found in chapter 5.

#### 3.3.2 Grid

A computer grid present at the MedUni Vienna was used for the simulation due to the high requirements on computing power. The mentioned grid is based on the MOCCAMED (MOnTe Carlo CACalculations in MEDicine) collaboration [22] used for computationally intensive clinical relevant research projects.

The aim of a grid is to split up computing jobs along different processors available to reduce computing time. A schematic picture of a grid with 4 nodes is given in figure 3.3. A central server manages the job distribution within grid by feeding the individual nodes and allocating storage space. Several computers present within the grid, including work stations or student PCs, can provide defined parts of their computing power dependent on their current requirements. This makes it possible to utilize unneeded computing power of different processors.

### 3.4 Image Reconstruction

#### 3.4.1 Data Manipulation

Prior to image reconstruction data manipulation had to be done to create processable data types for image reconstruction in STIR. A C++ source code (see external disk) developed by a research group from Jülich was used to read out the coincidence tree output from the gained GATE simulation .root file (ROOT [23] is a data analysis framework developed at CERN) and create the corresponding projection header files.

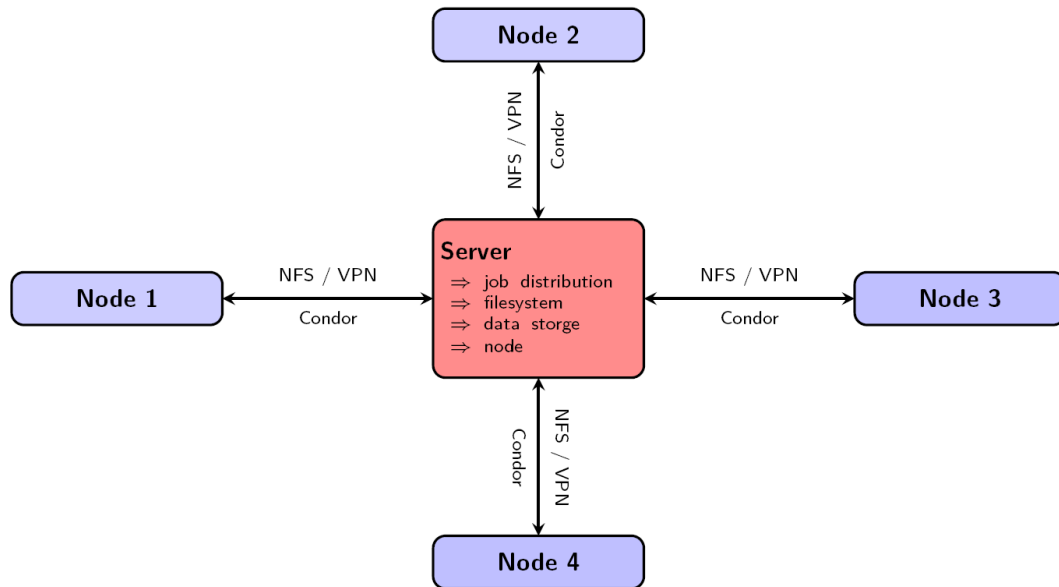


**Figure 3.3:** Visualisation of the Grid operation mode. A simulation is split up into different parts. The splits are being passed on to available processors within the network [Figure: Courtesy of A. Hirtl].

### 3.4.2 STIR

Image reconstruction of the simulation raw data was done with the program STIR (Software for Tomographic Image Reconstruction) [24], an open source software library for 3D reconstruction of raw PET data. It originated from the PARAPET project, a cooperation on 3D PET reconstruction funded by the European Union. This C++ library includes the usage of several reconstruction algorithms, scanner geometries, filters and other corrections.

FBP as well as iterative image reconstruction (OSEM), in this work, were executed with STIR.

Besides the projection data, FBP in STIR requires information about the applied filter. Furthermore arc correction is done. This refers to the fact that the space between LORs in the center of the PET system is larger than for LORs on the periphery.

The OSEM algorithm, in STIR called OSMAPOS, is based on input projection data, reconstructed with predefined parameters like the number of iterations and subsets (further information can be found in the parameter file on the external disk). The initial image

used for the OSEM algorithm in STIR is usually 1 for all voxels (3-dimensional pixel). Images are saved at predefined subiteration intervals.

## **3.5 Image Visualisation**

### **3.5.1 ImageJ**

For the visualisation of the reconstructed images, ImageJ, a java based open source tool for several tasks in image processing was used. It can read all the popular image formats as well as raw data like it was needed in this work. Summation of cross section images, projection on a certain coordinate plane, contrast manipulation, sharpening, smoothing or the creation and analysis of profile plots are a fractional amount of the facilities of this tool.

## 4 Simulation and Image Reconstruction

The following explanations should serve as a short instruction for the interested reader to be able to comprehend and reconstruct the procedures within this work. The most important steps and excerpts of some of the details of the executed simulation and image reconstruction are given to provide an insight into the structure of a simulation in GATE and accordingly into the operations of image reconstruction in STIR.

The entire source codes of the mentioned files in this chapter can be found on an external disc (except .root and projection data due to file sizes of several GB).

### 4.1 PET Simulation - GATE

A source code excerpt of the main file *My\_PET.mac* of the GATE simulation can be seen below. The individual parts of the main file are described subsequently:

```
# M y P E T

# V I S U A L I S A T I O N
/control/execute My_visu.mac

/gate/geometry/setMaterialDatabase GateMaterials.db

# W O R L D
/gate/world/geometry/setXLength 100. cm
/gate/world/geometry/setYLength 100. cm
/gate/world/geometry/setZLength 100. cm
```

```
# S Y S T E M
/control/execute My_system.mac

# P H A N T O M
/control/execute My_phantom.mac

# P H Y S I C S
/control/execute My_physics.mac

# D I G I T I Z E R
/control/execute digitizer.mac

# S O U R C E
/control/execute Y_source.mac
/control/execute backgroundsource.mac

# O U T P U T
/gate/output/root/enable
/gate/output/root/setFileName Ysource

# R A N D O M
/gate/random/setEngineName MersenneTwister
/gate/random/setEngineSeed auto

# S T A R T
/gate/application/setTimeStart 0.0 s
/gate/application/setTimeSlice 1 s
/gate/application/setTimeStop 1800 s
/gate/application/startDAQ
```

**# VISUALISATION** In this file the visualisation of the simulation can be enabled and defined. This includes the zoom factor and angle of observation of the PET system. Different steps of the visualisation of the simulation can be seen in the following figures (4.1-4.4).

**# WORLD** The world defines the volume where the simulation takes place (see figure 4.1). All the simulated processes inside the volume are taken into consideration. Photons leaving the world are not taken into account for the simulation anymore.

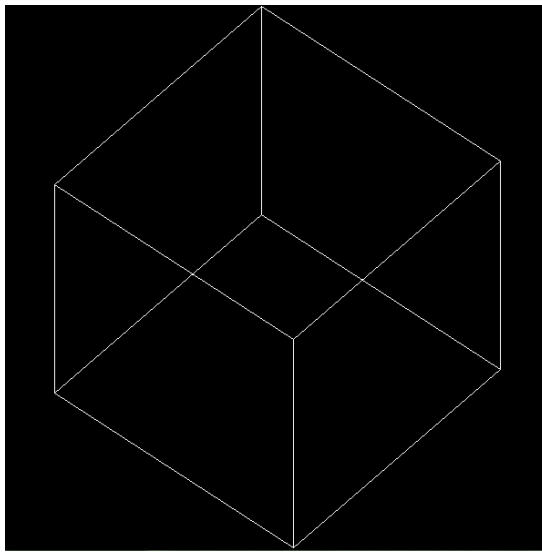


**Figure 4.1:** Visualisation of the world in GATE, where the simulation takes place. Photons leaving this volume are not being tracked further on.

**# SYSTEM** The geometry of the PET system is defined in this file. It contains information about the radius and length of the system as well as about the number, arrangement and material of the scintillating crystals. A visualisation of the individual steps of setting up the PET system can be found in figure 4.2.

**# PHANTOM** In the phantom module the surrounding of the source is defined. Referring to in vivo PET imaging this would be the human body, mainly consisting of water, bones and human tissue. These materials with their specific properties are present in the material database of GATE. Furthermore, the form and size of the phantom is defined. In figure 4.3 a cylindrical water phantom inside a PET system is shown.

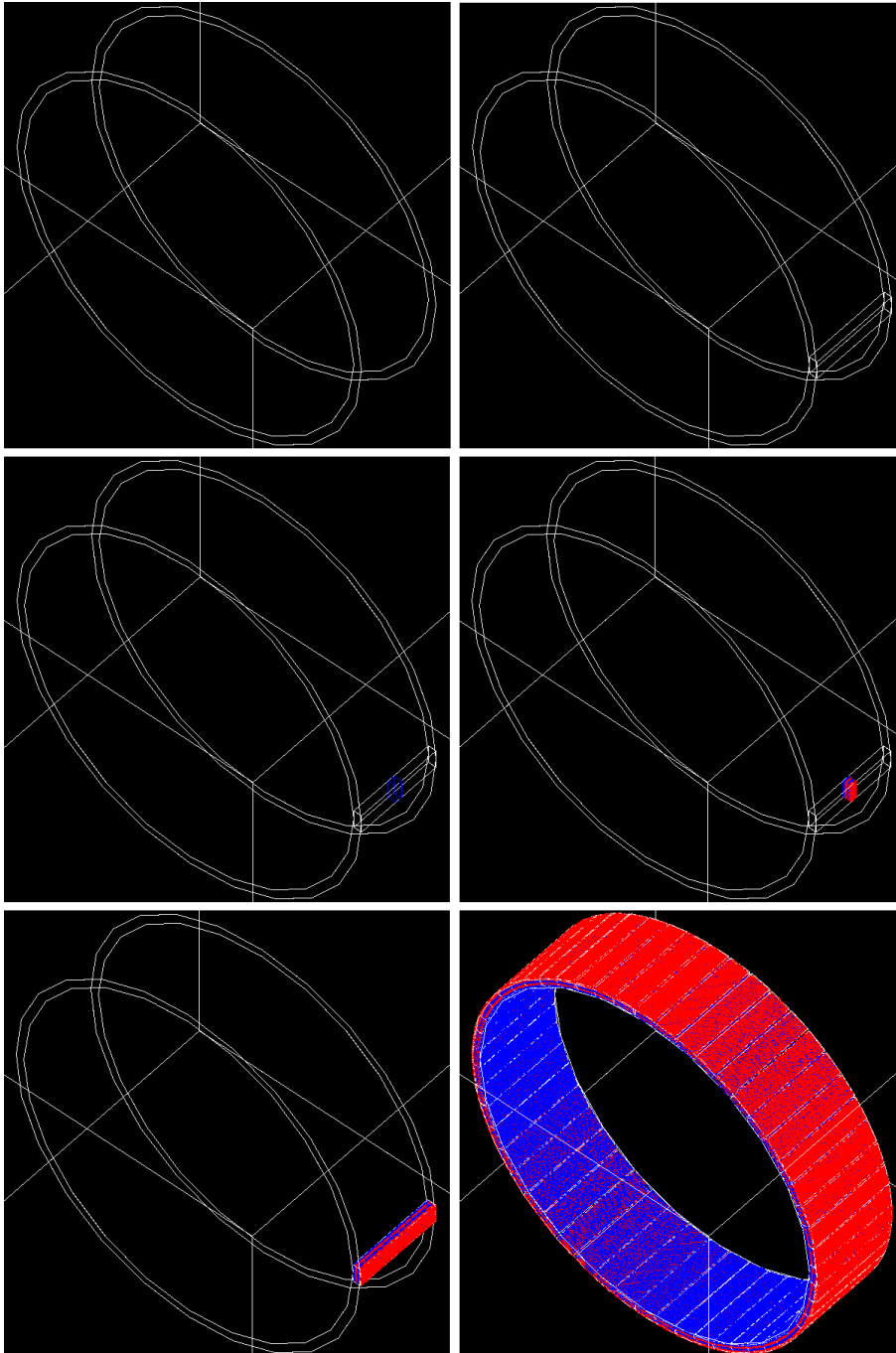


**Figure 4.2:** Progressive stages of building up a PET ring in GATE. At first, the defined empty PET ring is built up. A box volume is created, together with a smaller volume inside the box, corresponding to the crystal dimensions. The crystal is repeated over the box volume. Finally, the box volume is repeated along the ring.

**# P H Y S I C S** In this file all the physical interactions occurring in the simulation are defined. This includes important photon matter interactions like the photoelectric effect, Compton- and Rayleigh scattering as well as pair production and positron annihilation.

**# D I G I T I Z E R** The digitizer module is needed to define the way a hit in the detector is transformed into an actual signal. It includes, amongst others, detector properties like energy blurring, crystal light yield, quantum efficiency, energy window, coincidence- and dead time. It is needed to provide a realistic simulation of a specific PET system.

**# S O U R C E** All characteristics of the source are defined in this section. It includes the quantity, size, location and movement of the source as well as properties like decay form, half life and activity. A visualisation of a source configuration inside a simulated PET system can be found in figure 4.4.

The background of a radioactive source, observable in real PET images, is also defined in this section.

**# O U T P U T** The simulation data gained can be processed with several output formats. Depending on the aim of data manipulation the specific outputs can be enabled. In this thesis, the ROOT output, developed at CERN [23], was used for further investigation and image reconstruction using STIR.

**# R A N D O M** Within this file one can set up the starting point for the Monte Carlo simulation. For statistical reasons a random starting point was chosen to provide balanced results.

**# S T A R T** In this module the simulation is started. Furthermore, it inherits information on the simulation time and the number of splits. The simulation time can be adjusted to the time window in practical PET imaging.

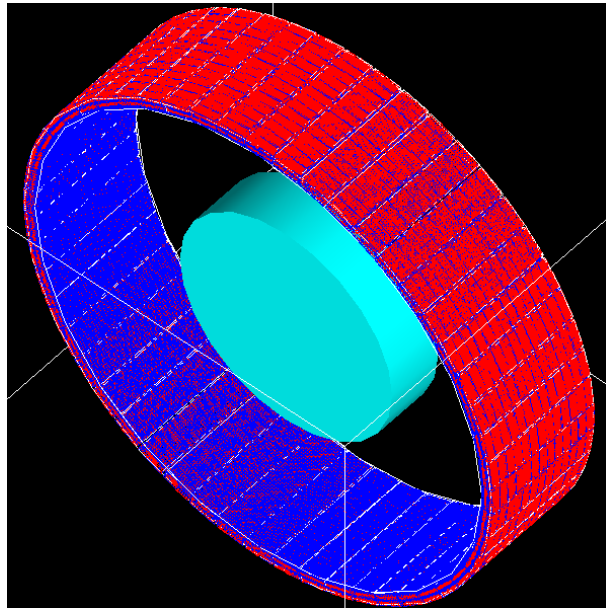


**Figure 4.3:** Visualisation of a cylindrical water phantom (cyan) inside a PET system (red/blue).

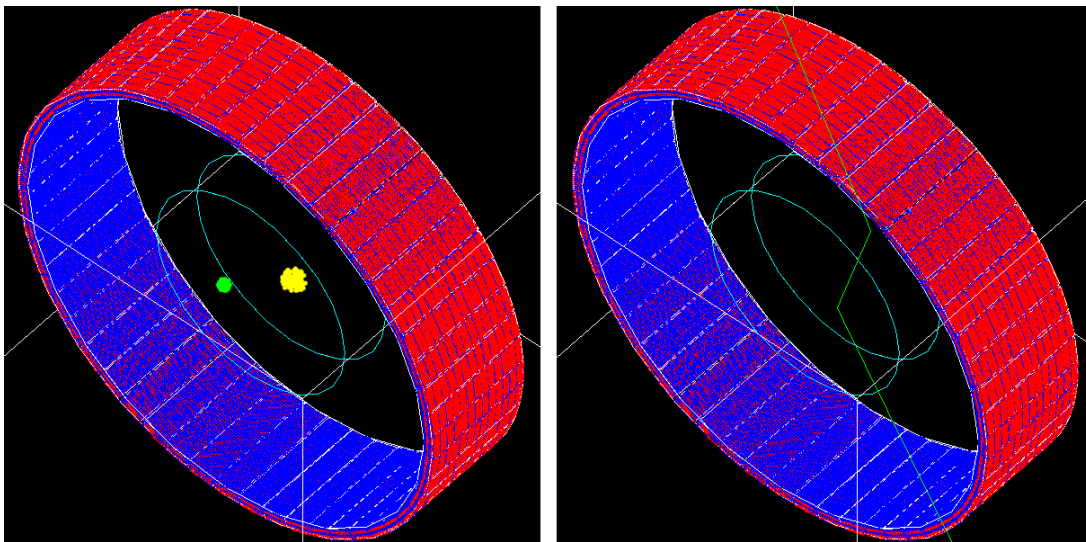


**Figure 4.4:** Left: Two sources (green, yellow) inside a water phantom (transparent cylinder) surrounded by a PET system (red/blue). Right: Possible annihilation photon paths due to scattering processes (green lines).

### 4.1.1 Submitting Simulation to Grid

The computational intensive simulations were sent to the grid with the command

```
sh submit2CondorGate62Short.sh
```

The submitting file includes the simulation file name and information about the number of splits. The number of splits equals the number of jobs sent to different processors within the grid, having a major impact on the duration of the simulation.

For example a simulation of a 10 minutes PET scan with 1 split is being executed by a single processor. A fragmentation of the same PET scan simulation time into 600 splits leads to 600 jobs being computed by different processors simultaneously, each inheriting 1 second of the PET scan simulation time. Theoretically, having sufficient processor capacities, this would reduce the simulation running time by a factor of 600.

The submitting file also declares job priorities and requirements for the available working stations.

## 4.2 Image Reconstruction - STIR

The simulation raw data was reconstructed with STIR, using FBP and an iterative (OSEM) algorithm.

For compatible reconstruction data types, the ROOT output files had to be modified using the C++ program from the Jülich research group. The created data was then used as an input for the implemented reconstruction algorithms in STIR. The execution files for the different algorithms include detailed information about the scanner geometry, filters and reconstruction properties.

For further information a detailed guideline on the individual steps mentioned is given in the appendix of this thesis.



# 5 Results and Discussion

## 5.1 Fluorine 18

Whilst  $^{90}\text{Y}$  is primarily used for cancer treatment due to a high deposition of energy,  $^{18}\text{F}$  is mainly used for PET imaging. Because of the superior image quality of  $^{18}\text{F}$  compared to  $^{90}\text{Y}$  PET imaging, an  $^{18}\text{F}$  simulation was executed to be able to test the basic functionality of the set up.

### 5.1.1 Simulation

The  $^{18}\text{F}$  sources were simulated over a period of 30 minutes with a specific activity of 20 kBq/ml. A predefined positron energy distribution within GATE was used. No background activity was used in this simulation. The energy resolution of the detector was set to 14% with a lower threshold of 380 keV and an upper threshold of 650 keV. No attenuation correction was executed. The detailed detector characteristics taken into consideration for the simulation can be found in the corresponding files on the external disk. At first the simulation data was evaluated:

The energy distribution of the detected annihilation photons can be seen in figure 5.1. It shows an expected maximum at the annihilation photon energy of 511 keV. A shift in the energy distribution to lower energies can be seen, resulting in an energy mean value of 498 keV. This can be explained by scattering events leading to a minimal loss of energy.

To verify and compare the individual source positions and sizes of the simulation data and the reconstructed image, the activity distribution for different projection axes of the  $^{18}\text{F}$  source was examined. This is shown in figures 5.2, 5.3 and 5.4. They illustrate the size and activity of the  $^{18}\text{F}$  sources along referring axes after the simulation. The activity distribution of the different projections is in agreement with the simulation data input.

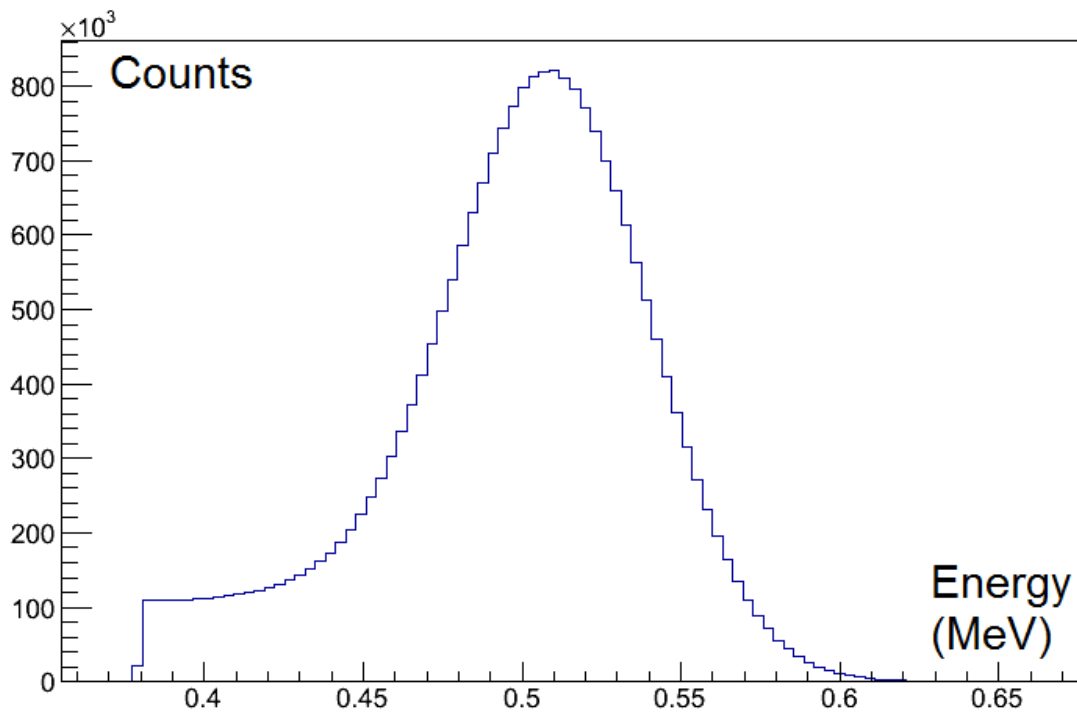


**Figure 5.1:** Energy distribution of the detected  $^{18}\text{F}$  annihilation photons. The energy cut off can be seen (specific activity: 20 kBq/ml, measurement time: 30 minutes).

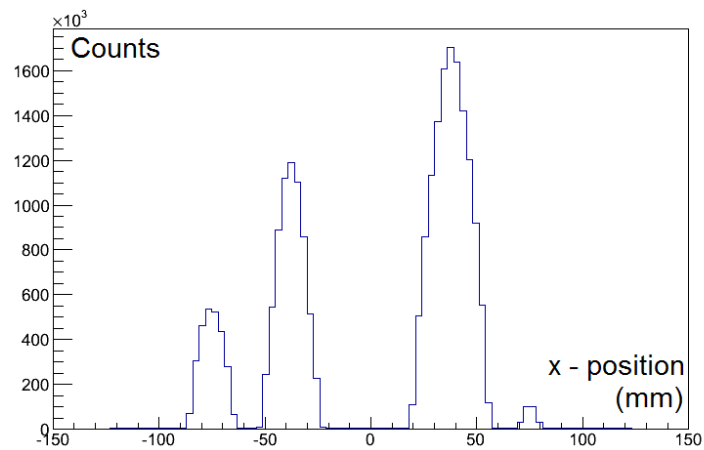


**Figure 5.2:** Source distribution of  $^{18}\text{F}$  sources along the x - axis (specific activity: 20 kBq/ml, measurement time: 30 minutes).

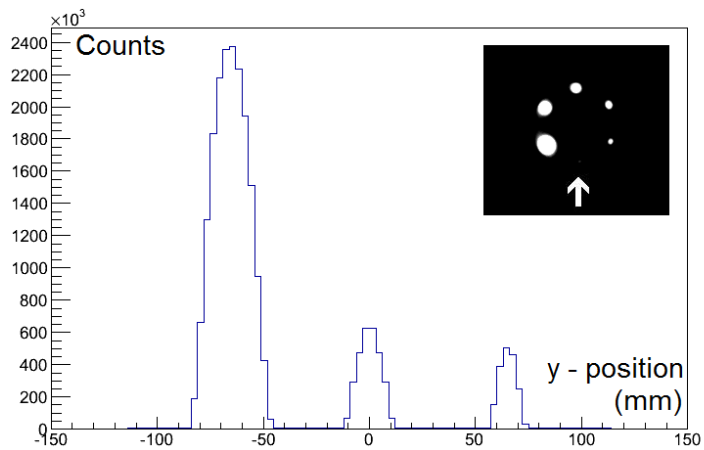


**Figure 5.3:** Source distribution of  $^{18}\text{F}$  sources on the y - axis with the corresponding reconstructed image (specific activity: 20 kBq/ml, measurement time: 30 minutes). The y - projection is visualized by the white arrow.

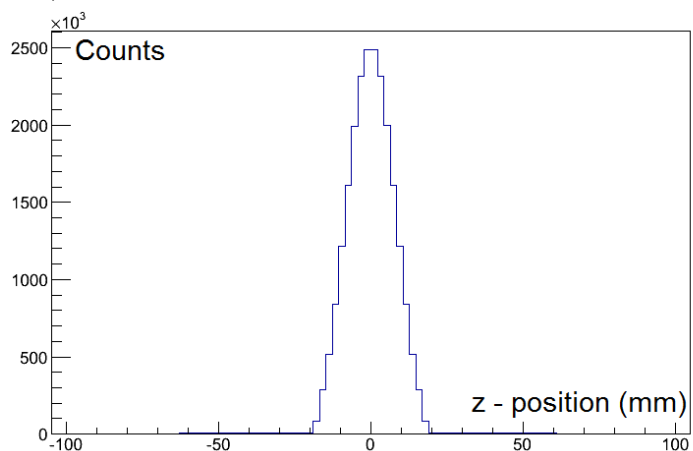


**Figure 5.4:** Source distribution of  $^{18}\text{F}$  sources on the z - axis (specific activity: 20 kBq/ml, measurement time: 30 minutes).

## 5.1.2 Image Reconstruction

The results of the  $^{18}\text{F}$  image reconstruction of the simulated raw data are shown in the following sections.

### 5.1.2.1 Filtered Back Projection

At first, the FBP algorithm was carried out with a simple ramp filter. No further filters were applied. The calculation time for image reconstruction using this method was in the range of a few seconds. The reconstructed image is shown in figure 5.5 together with a 3D visualisation in figure 5.6. Each of the 6 defined sources can be identified clearly.

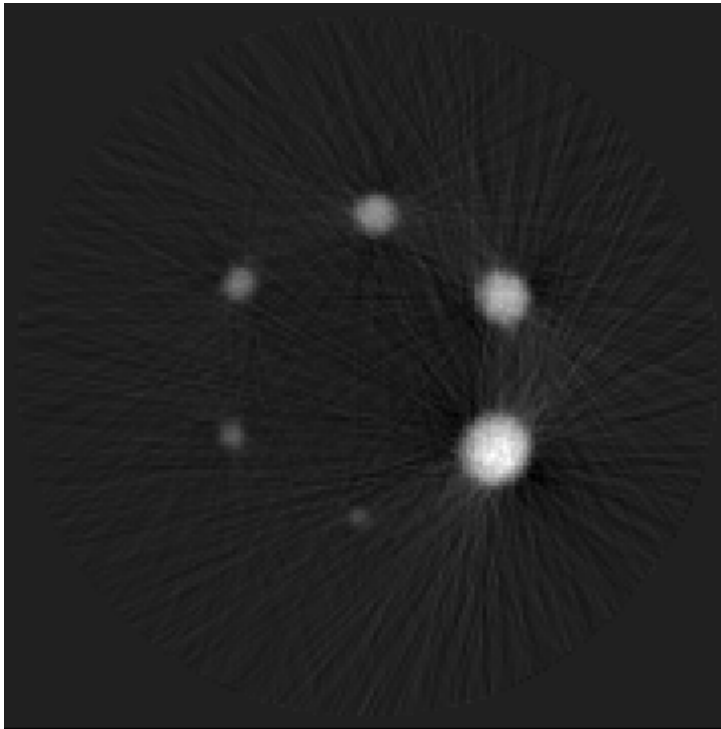


**Figure 5.5:** Reconstructed image of multiple  $^{18}\text{F}$  sources using FBP (specific activity: 20 kBq/ml, no background activity, measurement time: 30 minutes). All of the sources can be identified.

Common disadvantages of this simple reconstruction method can be seen. Artefacts resulting from individual LORs appear and would need to be eliminated by further filtering methods. FBP is not the first choice for clinical image reconstruction based on a lack of image quality.

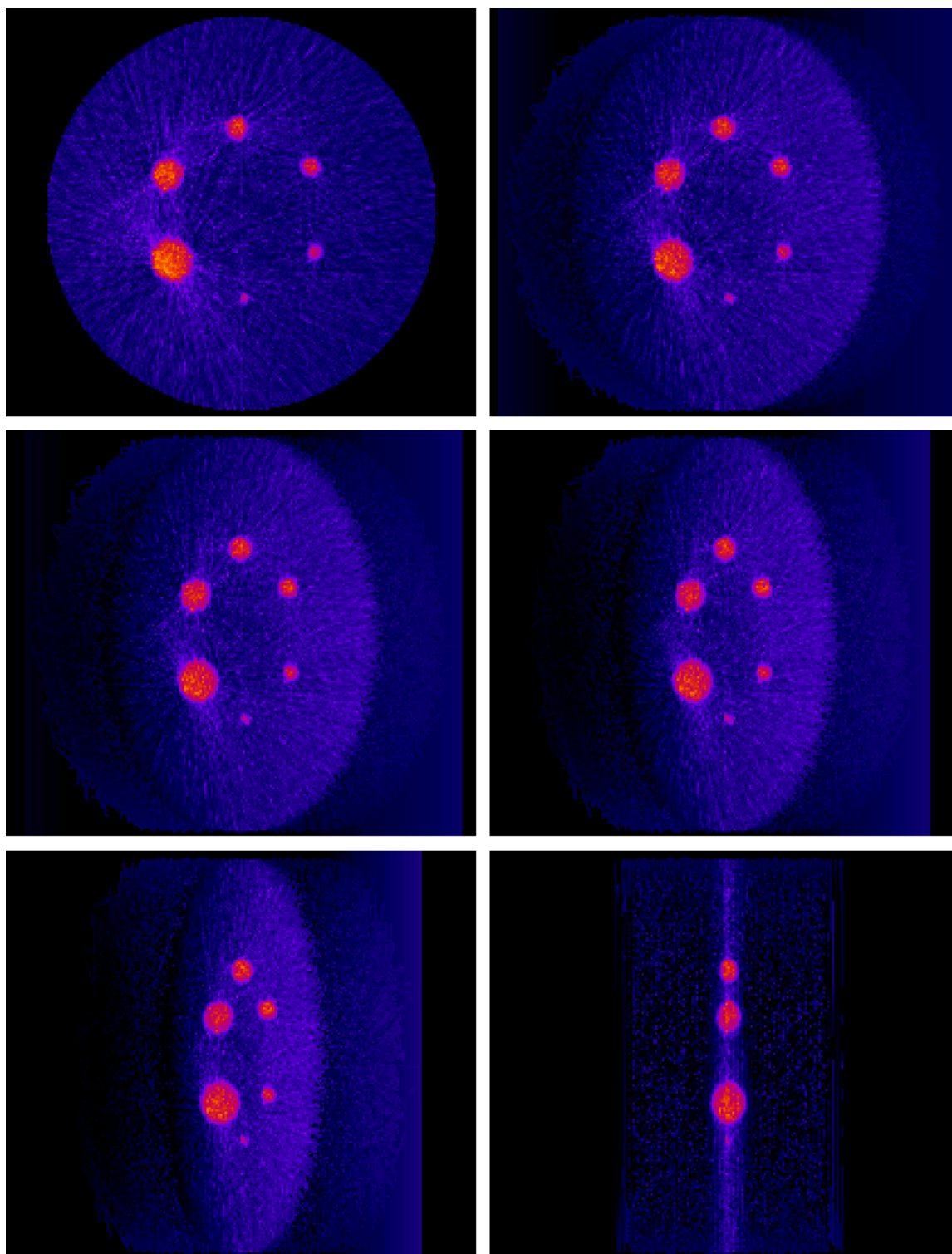


**Figure 5.6:** 3D visualisation of the FBP reconstructed  $^{18}\text{F}$  PET simulation using a color filter (specific activity: 20 kBq/ml, no background activity, measurement time: 30 minutes).

### 5.1.2.2 Iterative Reconstruction

For the iterative reconstruction method the same simulation raw data was used as for the FBP. 4 iterations and 12 subsets were executed for reconstructing the image. As this method requires a large amount of computing power, the image reconstruction time was in a range of approximately 30 minutes. Testing with a single subset led to a reconstruction time of several hours.

The result of the iteratively reconstructed image and a 3D visualisation are shown in figures 5.7 and 5.8, respectively. They reveal an enormous improvement in image quality compared to the method of FBP. Although no attenuation correction was applied, the location and contours of the single source volumes can be identified precisely. Even the smallest source with a diameter of 10 mm is visible quite clearly.

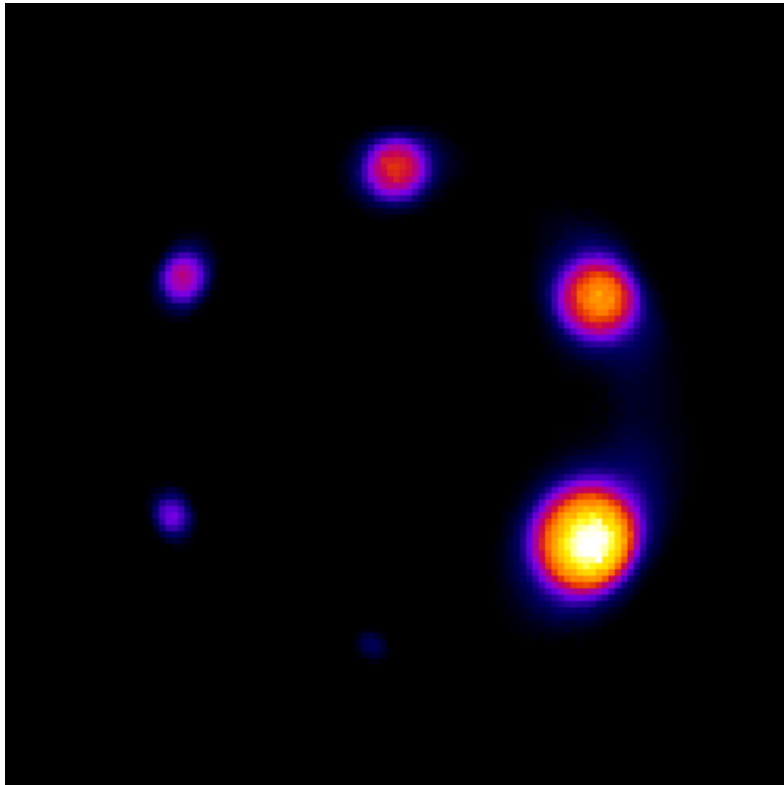


**Figure 5.7:** Iteratively reconstructed image of multiple  $^{18}\text{F}$  sources using 4 iterations and 12 subsets. Light colours contribute to high activities whilst darker colours contribute to lower activities (specific activity: 20 kBq/ml, no background activity, measurement time: 30 minutes). Iterative image reconstruction leads to an improvement in image quality compared to FBP.

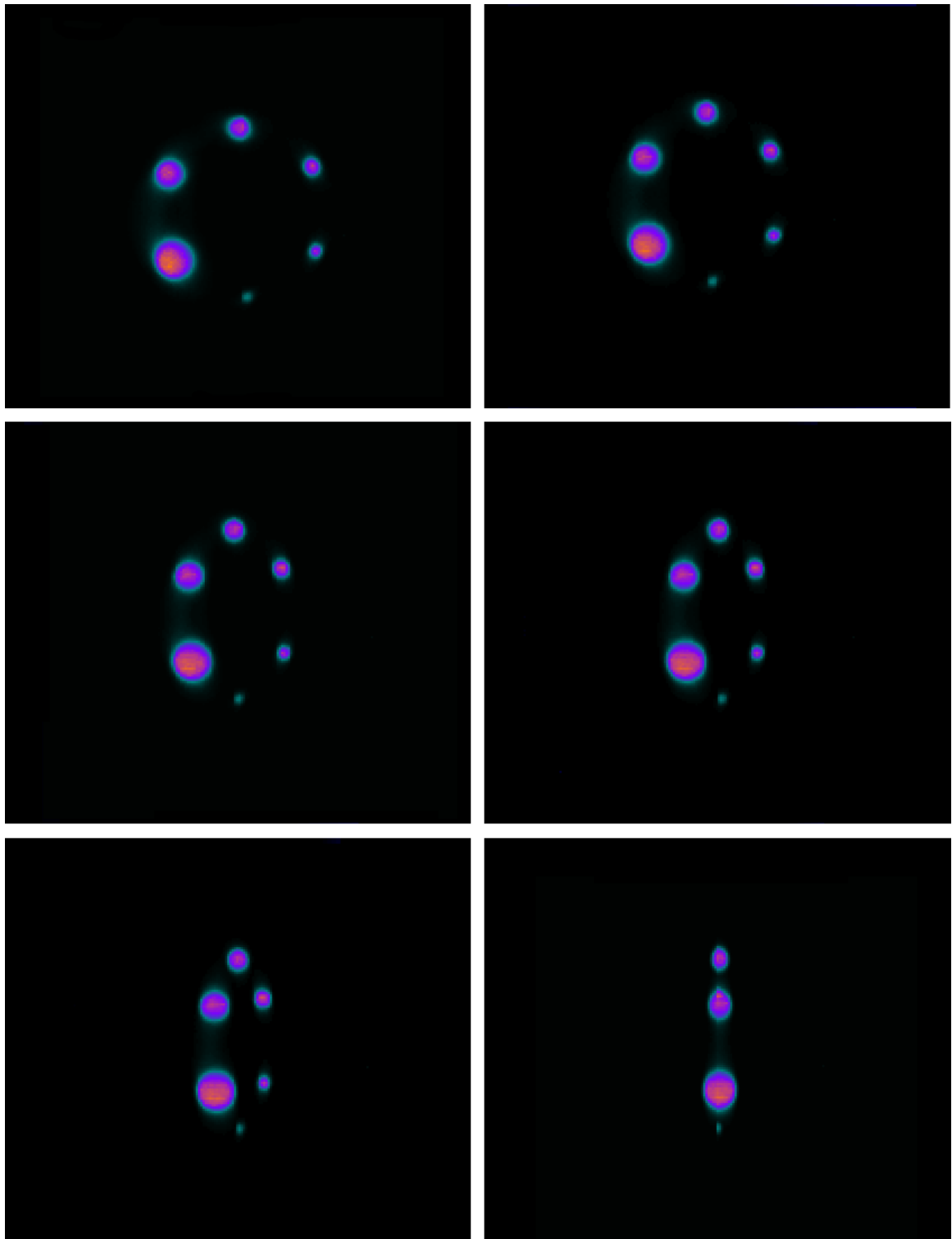


**Figure 5.8:** 3D visualisation of the iteratively reconstructed  $^{18}\text{F}$  PET simulation with a specific activity of 20 kBq/ml and a measurement time of 30 minutes. 4 iterations and 12 subsets were used.

**Number of Iterations** As described in the second chapter, the product of the number of iterations and subsets has a major impact on the final image quality. In clinical practice one has to find a compromise between an acceptable computing time and image quality. The different image contrast concerning a diverse number of iterations can be seen in figures 5.9 - 5.12. The grey values along a certain line of reference (yellow) for a defined number of iterations (1-4) are shown. An increase in the number of iterations leads to a better image contrast and higher grey values. The number of subsets (12) was not changed.

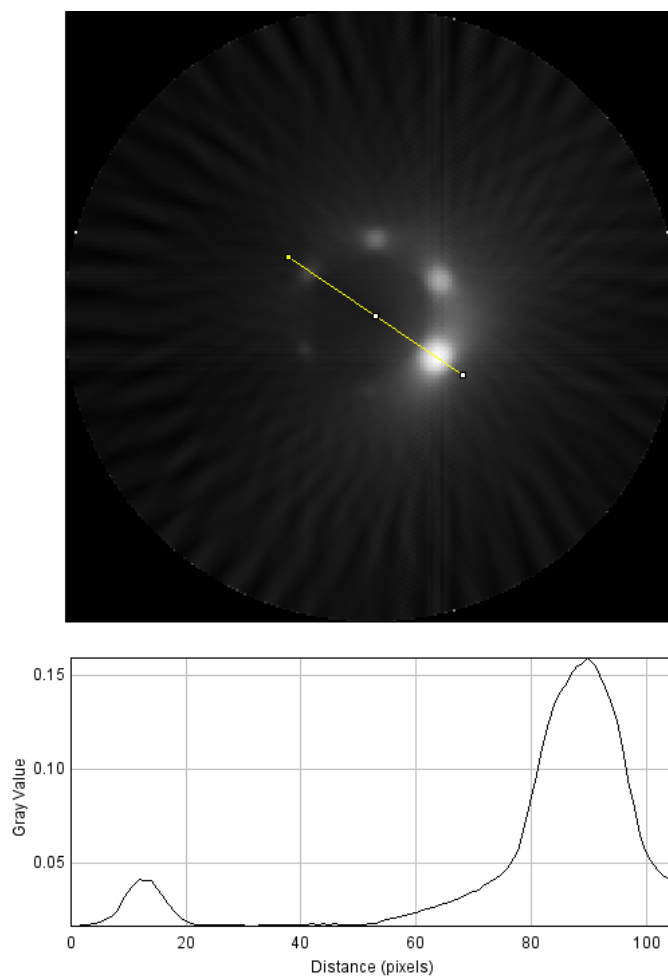


**Figure 5.9:** Reconstructed image of  $^{18}\text{F}$  sources with 1 iteration and 12 subsets. Grey values are shown for a certain line of reference (yellow). Image artefacts result from just a single image guess after 1 iteration.

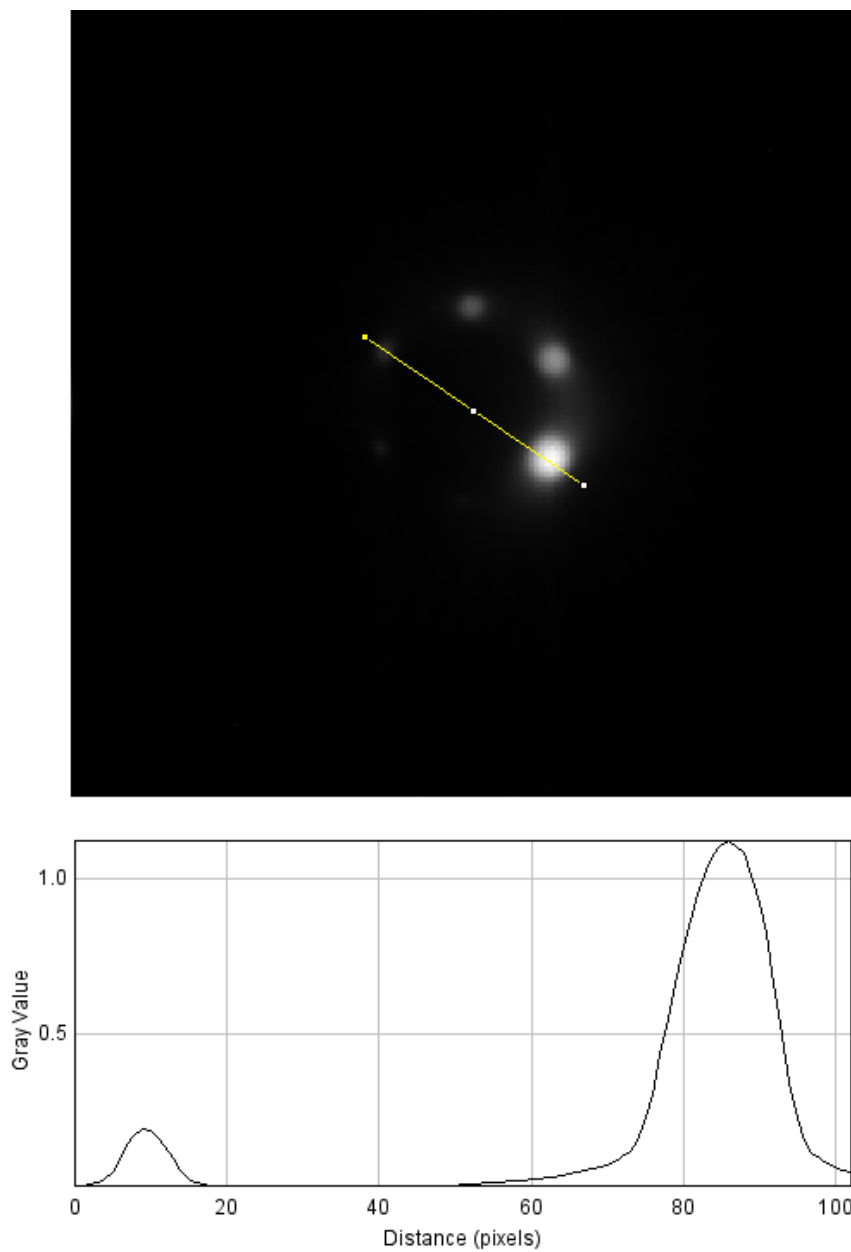


**Figure 5.10:** Reconstructed image of  $^{18}\text{F}$  sources with 2 iterations and 12 subsets. Grey values are shown for a certain line of reference (yellow). Artefacts were corrected using a second iteration. Contrast and grey values are enhanced.

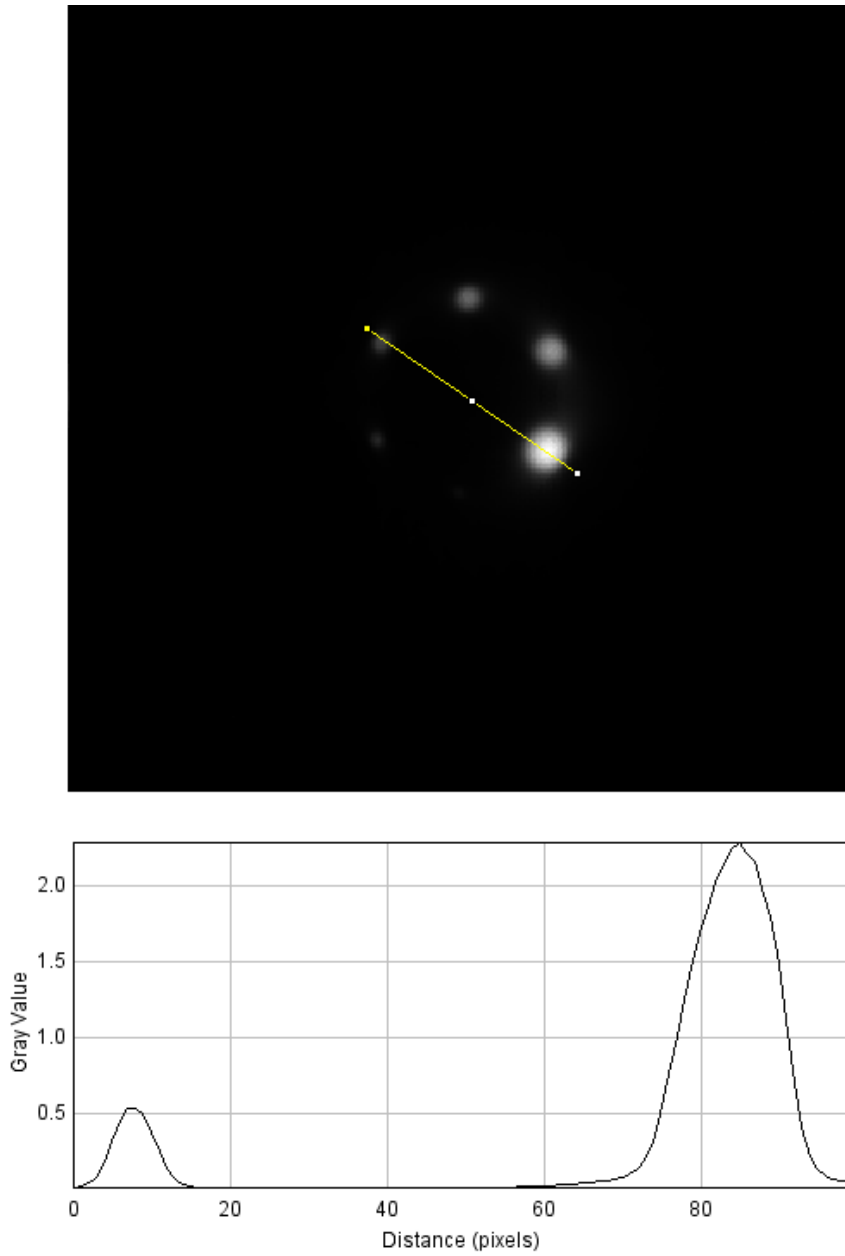


**Figure 5.11:** Reconstructed image of  $^{18}\text{F}$  sources with 3 iterations and 12 subsets. Grey values are shown for a certain line of reference (yellow). Further increase in the number of iteration leads to a better image contrast.

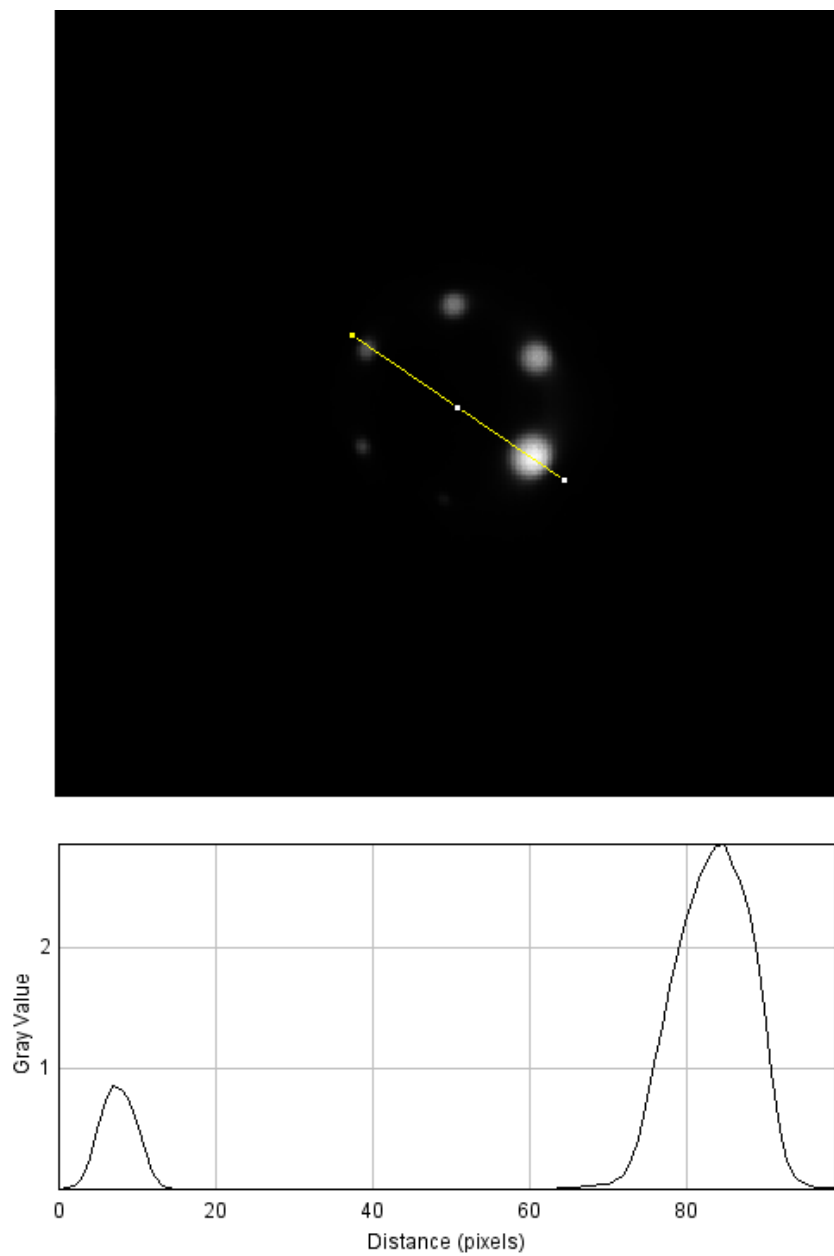


**Figure 5.12:** Reconstructed image of  $^{18}\text{F}$  sources with 4 iterations and 12 subsets. In comparison to lower iteration numbers the contrast and total gray value is increased for the depicted line of reference (yellow).

## 5.2 Yttrium 90

### 5.2.1 Simulation

Sensitivity in PET imaging is defined as  $S = \frac{C}{t \cdot A}$ .  $C$  refers to the number of detected photons,  $A$  stands for the source activity (kBq) and  $t$  stands for the time (seconds). In  $^{90}\text{Y}$  PET imaging sensitivity is reduced by a factor of  $10^{-5}$  compared to  $^{18}\text{F}$  PET imaging [3]. For this reason  $^{90}\text{Y}$  measurements and simulations require higher specific activities. Typical values are in a range of several MBq/ml.

In this thesis two simulation runs with  $^{90}\text{Y}$  were executed. The first one was carried out with a specific activity of 40 MBq/ml. This specific activity is higher than the ones used for clinical  $^{90}\text{Y}$  measurements. That was done to proof the general functionality of  $^{90}\text{Y}$  PET simulation. No background activity was used.

The second run was executed with a specific activity of 4 MBq/ml which is within the previously explained activity range used for real  $^{90}\text{Y}$  PET phantom measurements. For a realistic simulation of the  $^{90}\text{Y}$  distribution, the phantom background activity was set to 1/8 of the source activity, leading to 0.5 MBq/ml.

Both runs were carried out with a simulated measurement time of 30 minutes with no attenuation correction applied in image reconstruction. The  $^{90}\text{Y}$  positron energy distribution was approximated by mono energetic positrons with an energy of 369 keV. The energy resolution of the detector was set to 14%, with a lower threshold of 380 keV and an upper threshold of 650 keV.

The  $^{90}\text{Y}$  energy distributions of the detected coincidence photons from the 4 MBq/ml and the 40 MBq/ml simulations can be seen in figures 5.13 and 5.14, respectively, showing the same expected characteristics as the  $^{18}\text{F}$  energy distribution. The peak is located at approximately 511 keV, corresponding to the energy of an annihilation photon. The energy distribution is slightly shifted to lower energies by reasons of scattering processes leading to a mean value of approximately 500 keV.

The total count rate for  $^{90}\text{Y}$  is much lower than for the  $^{18}\text{F}$  simulation even though  $^{90}\text{Y}$  was simulated with a higher specific activity. This can be explained by the mentioned reduction in sensitivity based on the small branch ratio of  $^{90}\text{Y}$  leading to positron emission. The activity distribution of the 4 MBq/ml simulation projected along the different co-

ordinate axes can be seen in figures 5.15 - 5.17. The influence of the background on the activity distribution can be seen since the sources are partly masked by the background activity. In comparison to that, the activity distribution of the 40 MBq/ml simulation in figures 5.18 - 5.20 shows no background activity.

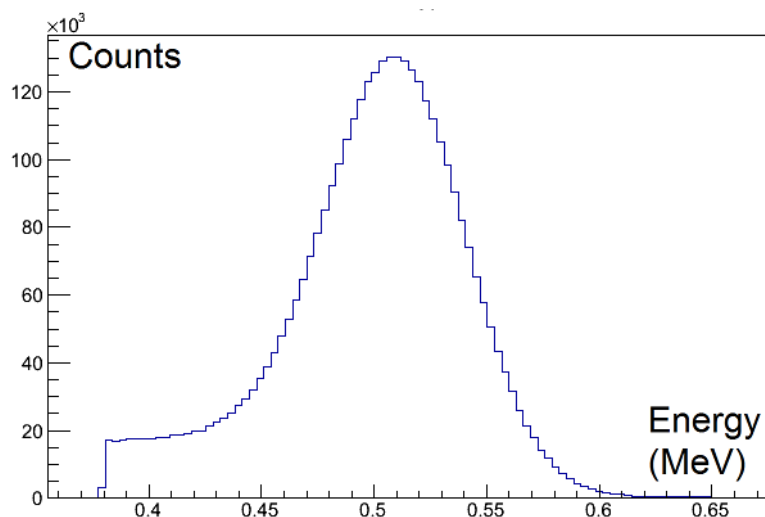


**Figure 5.13:** Energy distribution of the detected  $^{90}\text{Y}$  annihilation photons (specific activity: 4 MBq/ml, measurement time: 30 minutes).

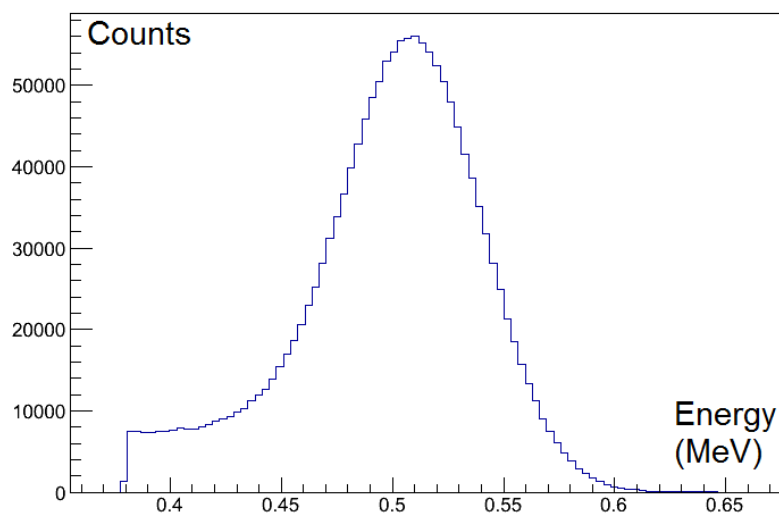


**Figure 5.14:** Energy distribution of the detected  $^{90}\text{Y}$  annihilation photons (specific activity: 40 MBq/ml, measurement time: 30 minutes).

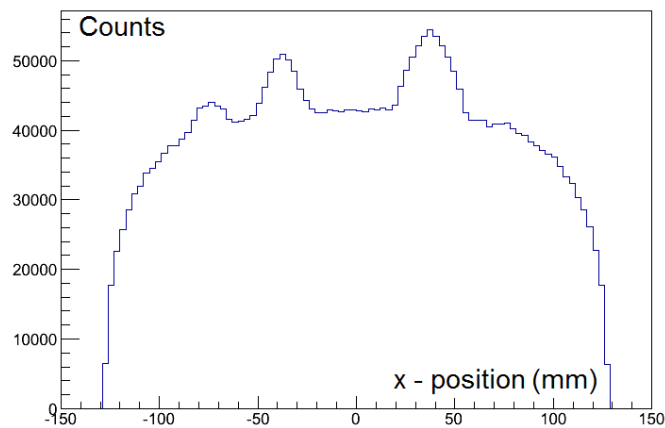


**Figure 5.15:** Distribution of  $^{90}\text{Y}$  sources along the x - axis (specific activity: 4 MBq/ml, background activity: 0.5 MBq/ml, measurement time: 30 minutes).

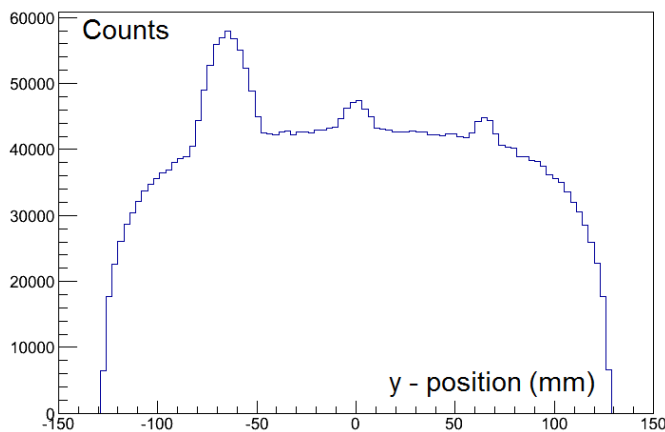


**Figure 5.16:** Distribution of  $^{90}\text{Y}$  sources along the y - axis (specific activity: 4 MBq/ml, background activity: 0.5 MBq/ml, measurement time: 30 minutes).

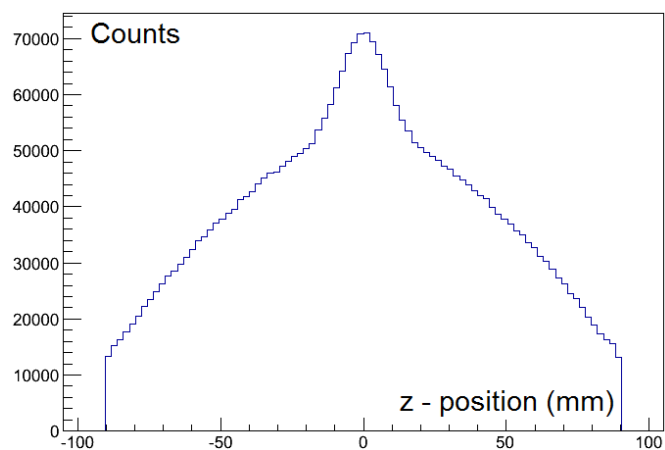


**Figure 5.17:** Distribution of  $^{90}\text{Y}$  sources along the z - axis (specific activity: 4 MBq/ml, background activity: 0.5 MBq/ml, measurement time: 30 minutes).

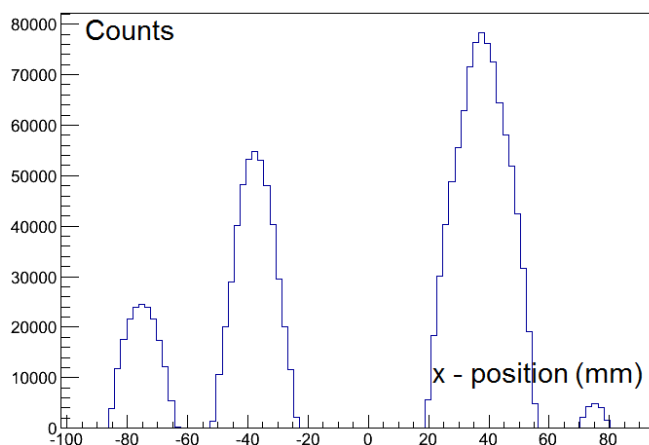


**Figure 5.18:** Distribution of  $^{90}\text{Y}$  sources along the x - axis (specific activity: 40 MBq/ml, no background activity, measurement time: 30 minutes).

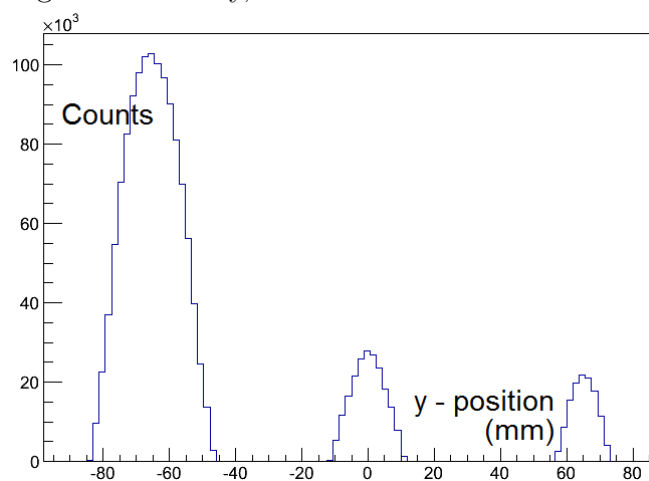


**Figure 5.19:** Distribution of  $^{90}\text{Y}$  sources along the y - axis (specific activity: 40 MBq/ml, no background activity, measurement time: 30 minutes).

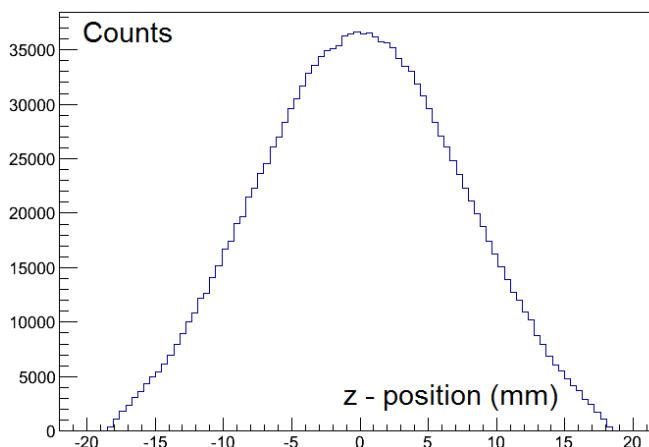


**Figure 5.20:** Distribution of  $^{90}\text{Y}$  sources along the z - axis (specific activity: 40 MBq/ml, no background activity, measurement time: 30 minutes).

## 5.2.2 Image Reconstruction

The resulting reconstructed images of  $^{90}\text{Y}$  based on the illustrated simulation data are shown and analysed in the following sections.

### 5.2.2.1 Filtered Back Projection

As for  $^{18}\text{F}$ , a simple ramp filter was used for the FBP reconstruction method.

The reconstructed  $^{90}\text{Y}$  image with a specific activity of 40 MBq/ml, no background and a PET scan simulation time of 30 minutes using FBP is shown in figure 5.21. Even though the image suffers from uncorrelated artefacts due to the nature of FBP, all of the sources are visible.

In figure 5.22, the reconstructed  $^{90}\text{Y}$  image for the realistic simulation with 4 MBq/ml, a background activity of 0.5 MBq/ml and a PET scan simulation time of 30 minutes is presented. It shows an enormous decrease in image quality compared to the 40 MBq/ml simulation since only the largest source (26.5 ml) is partly visible. This can be explained by the reduction of the specific activity by a factor of 10 and the implementation of background activity resulting in a lower image contrast. The non-included attenuation correction results in a highlighted phantom border and a lowered intensity in the center. Photons coming from the center have to traverse a longer path through the phantom and therefore are being attenuated more than photons from the outer regions of the phantom.

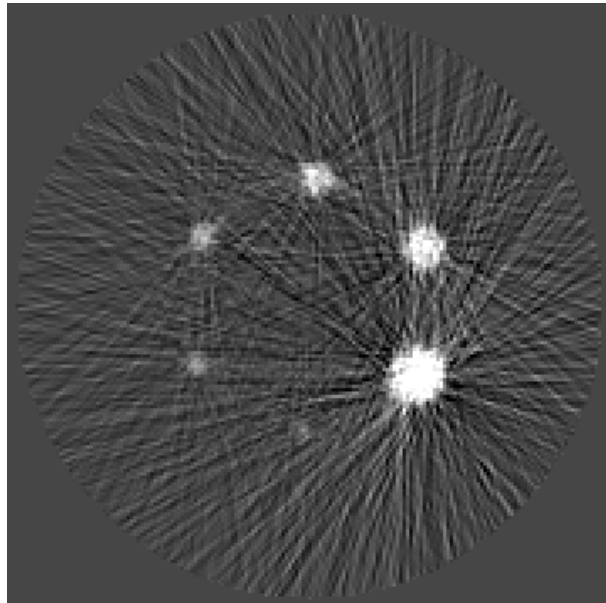


**Figure 5.21:** Reconstructed  $^{90}\text{Y}$  image using FBP (specific activity: 40 MBq/ml, no background activity, PET scan simulation time: 30 minutes). All the individual sources can be identified.

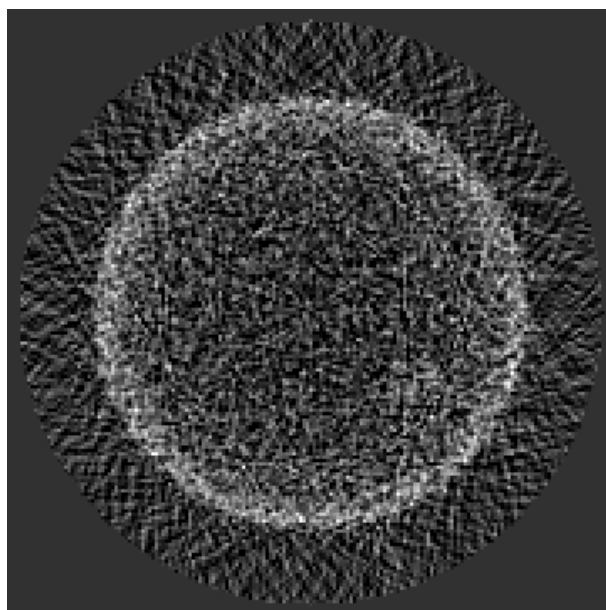


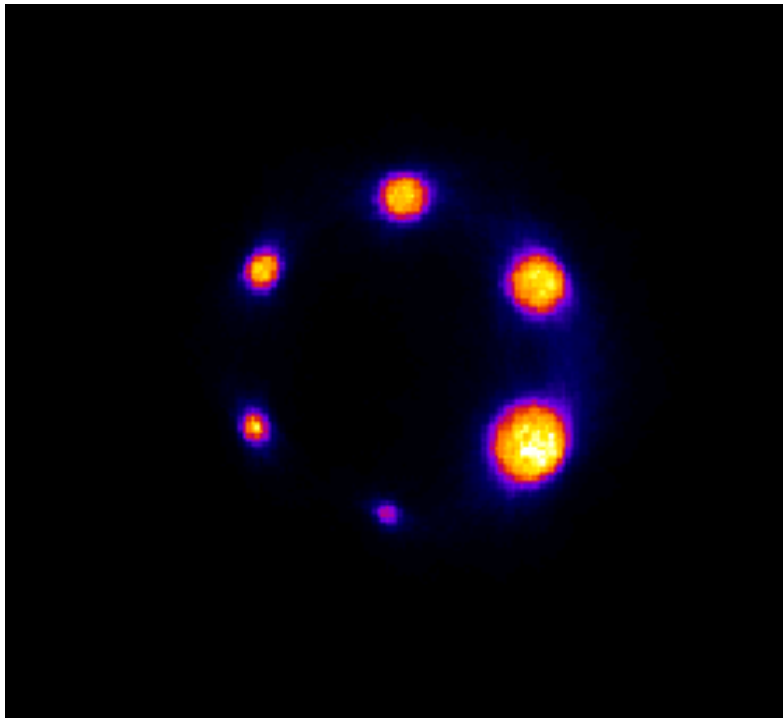
**Figure 5.22:** Reconstructed  $^{90}\text{Y}$  image using FBP (specific activity: 4 MBq/ml, background activity: 0.5 MBq/ml, PET scan simulation time: 30 minutes). No source can be identified clearly. The highlighted periphery compared to the center of the phantom is based on the lack of attenuation correction.

### 5.2.2.2 Iterative Image Reconstruction

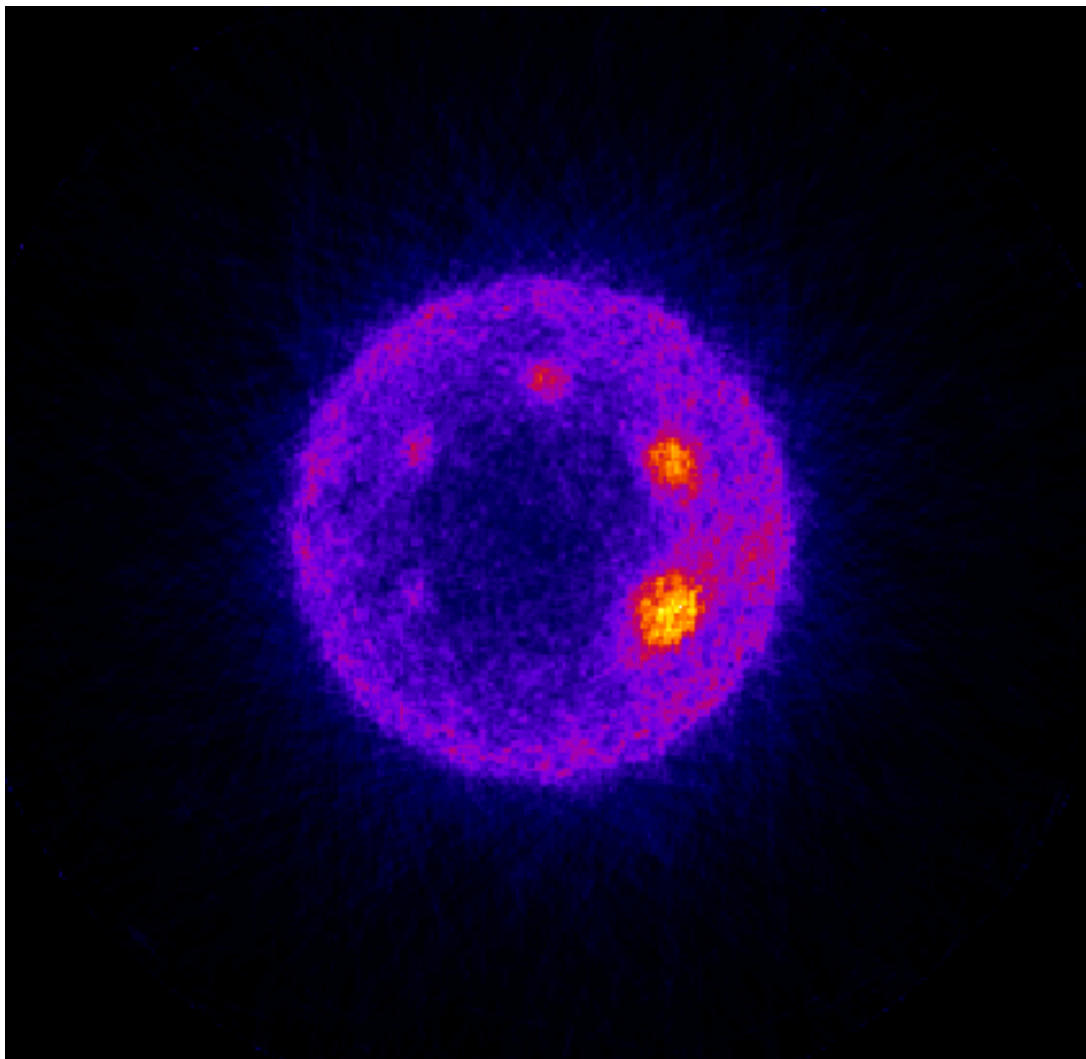
As for  $^{18}\text{F}$ , the iterative reconstruction of the  $^{90}\text{Y}$  PET simulation was executed with 4 iterations, using 12 subsets and no attenuation correction. The same simulation raw data were used as for the FBP.

Iterative image reconstruction of the 40 MBq/ml simulation (see figure 5.23) leads to an improvement in image quality compared to FBP (see figure 5.21). All of the individual sources can be identified clearly. The functionality of the  $^{90}\text{Y}$  simulation and image reconstruction can be confirmed.

The iteratively reconstructed image of the 4 MBq/ml simulation (figure 5.24) also shows an improvement in image quality compared to FBP (see figure 5.22). 5 of the 6 sources can be identified with this reconstruction method. The smallest source (diameter: 1 cm) is not visible clearly due to the influence of the background activity. The highlighted phantom border compared to the center, resulting from the lack of attenuation correction, is visible.

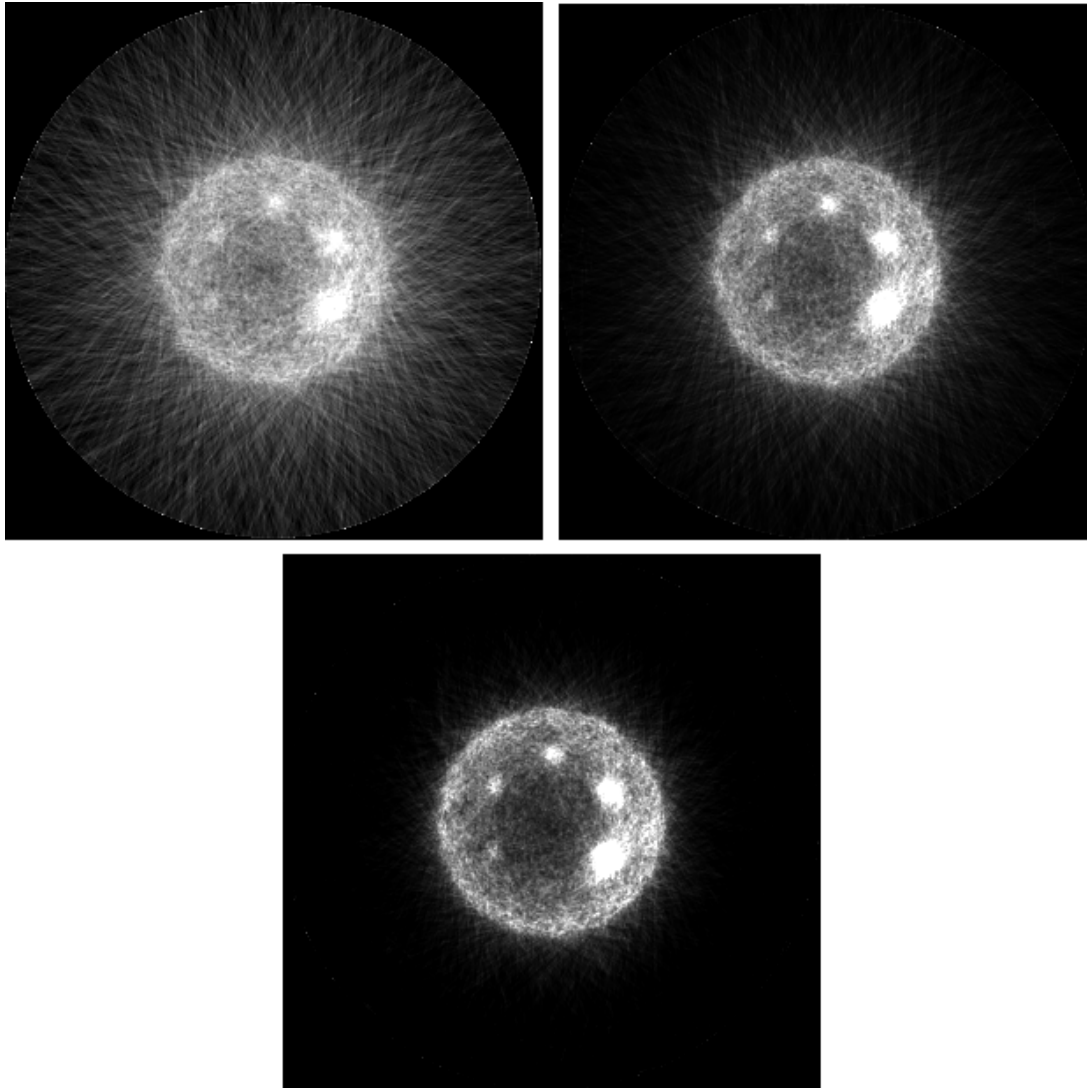


**Figure 5.23:** Iteratively reconstructed  $^{90}\text{Y}$  image using 4 iterations and 12 subsets (specific activity: 40 MBq/ml, no background activity, measurement time: 30 minutes). All of the sources can be identified clearly.



**Figure 5.24:** Iteratively reconstructed  $^{90}\text{Y}$  image frame using 4 iterations and 12 subsets (specific activity: 4 MBq/ml, background activity: 0.5 MBq/ml, measurement time: 30 minutes). At least 5 of the 6 sources can be identified. The periphery of the phantom is highlighted compared to the center since no attenuation correction was applied.

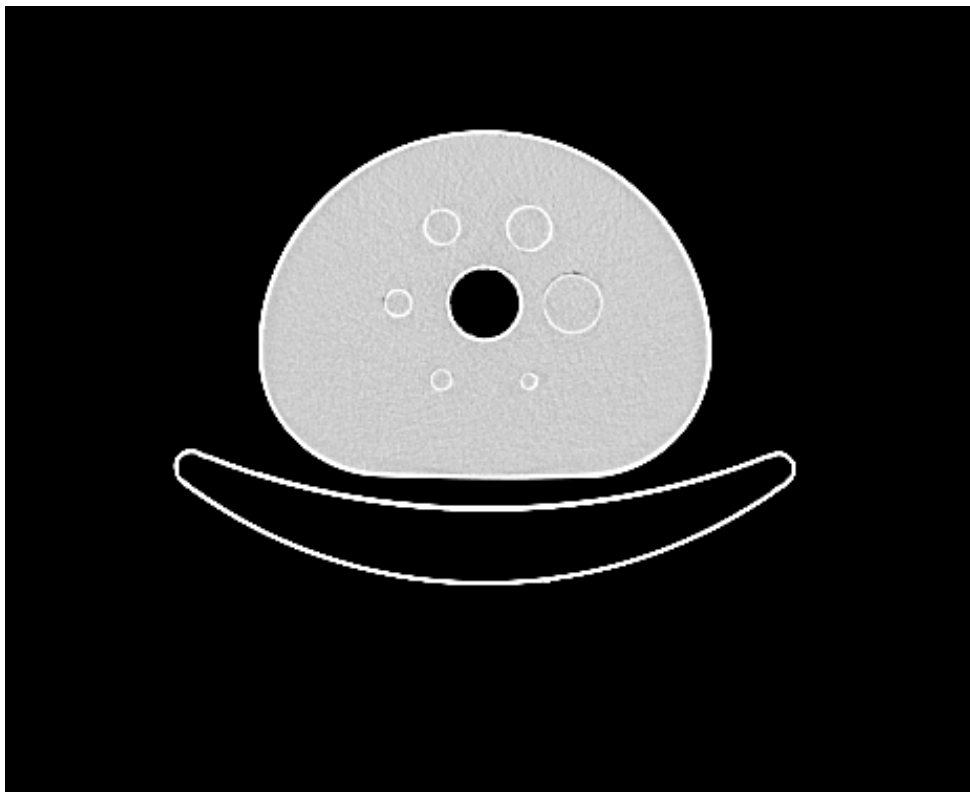
**Number of Iterations** An impressive improvement of the reconstructed image quality using a higher number of iterations can be seen in figure 5.25. Just using 1 iteration leads to a multiplicity of image artefacts. An increase in the number of iterations gradually eliminates these artefacts.



**Figure 5.25:** 4 MBq/ml  $^{90}\text{Y}$  image dependent on the number of iterations and subsets (12). 1 iteration (upper left), 2 iterations (upper right), 3 iterations (lower image)

## 6 Y90 - Phantom Measurements

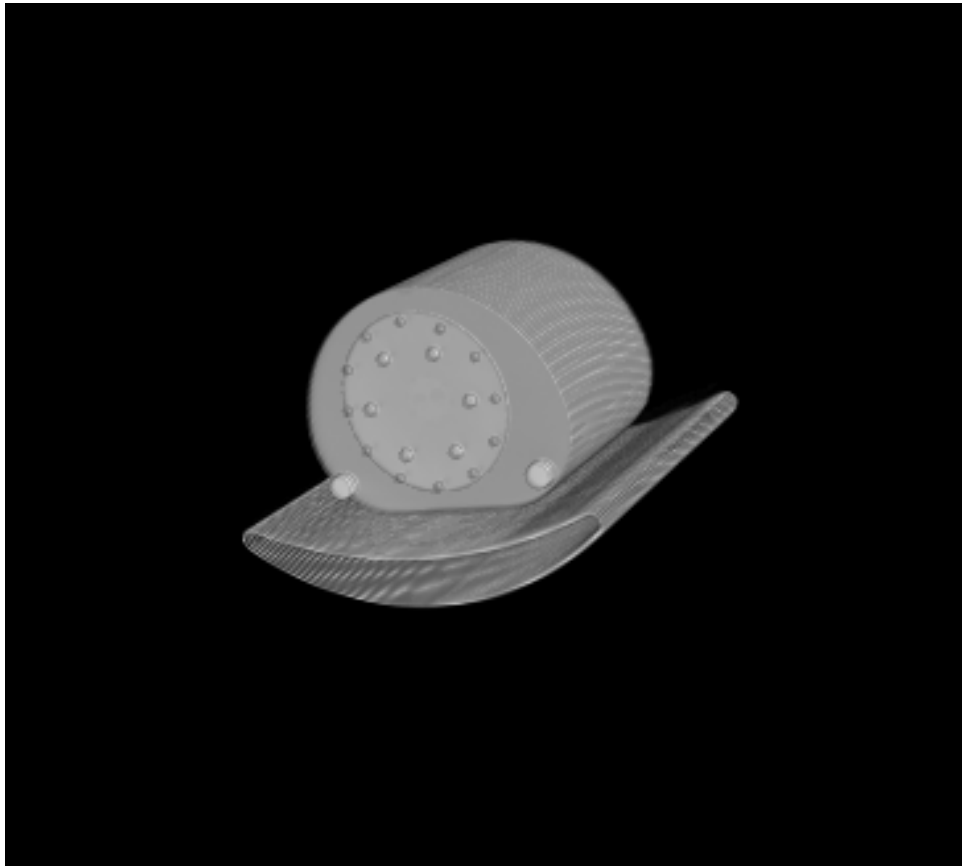
Realistic  $^{90}\text{Y}$  phantom measurements are provided by the nuclear medical research group at the MedUni Vienna and are based on the NEMA IEC body phantom. For these measurements an overall activity of 3.6 GBq  $^{90}\text{Y}$  was mixed with 1000 ml of water, leading to a specific activity of 3.6 MBq/ml. The 6 spheres were filled and the rest of the  $^{90}\text{Y}$  water mixture was added to the water filled phantom to simulate background activity occurring in real patient measurements.



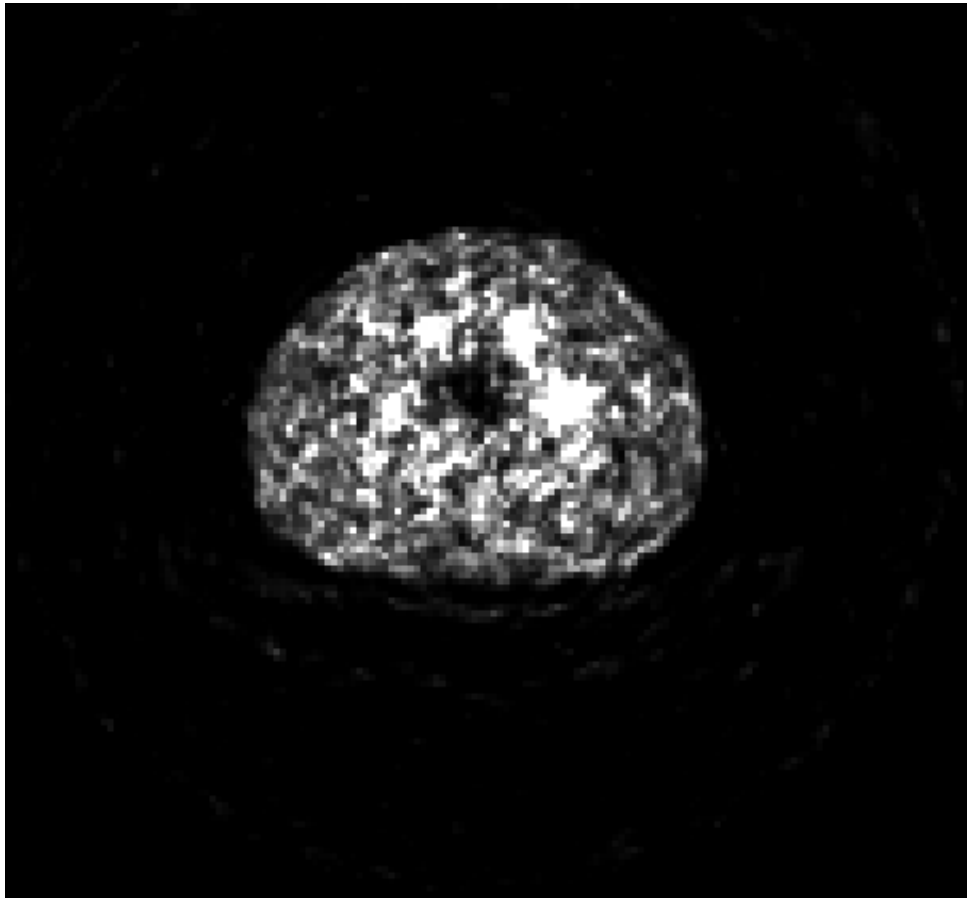
**Figure 6.1:** Sectional CT view of the phantom used for  $^{90}\text{Y}$  PET measurements.

Figure 6.1 shows a sectional CT view of the used phantom. The 6 sphere reservoirs for radionuclide source positioning are visible. A 3D image of the same phantom can be seen in figure 6.2. The bed under the phantom is also displayed.

The  $^{90}\text{Y}$  phantom PET image with a specific activity of 3.6 MBq/ml can be seen in figure 6.3. It shows a sectional view of the activity distribution, revealing the poor image quality of an  $^{90}\text{Y}$  PET scan. Still, 4 of the 6 sources can be identified. Due to rather low statistics the smallest spheres cannot be seen in this image. The  $^{90}\text{Y}$  simulation (specific activity: 4 MBq/ml, background activity: 0.5 MBq/ml) within this thesis shows similar results concerning image quality.



**Figure 6.2:** 3D visualisation of the used phantom based on NEMA IEC body phantom.



**Figure 6.3:** Sectional PET image view of  $^{90}\text{Y}$  sources with a specific activity of 3.6 MBq/ml. At least 4 out of 6 sources can be seen.



# 7 Summary and Outlook

**Summary** A complete PET model for the research on  $^{90}\text{Y}$  SIRT efficiency could be set up. This includes the realistic simulation of a present PET device at the MedUni Vienna with specific known data and characteristics as well as the process of image reconstruction of the gained simulation data.

Simulation and image reconstruction using  $^{18}\text{F}$  (specific activity: 20 kBq/ml, measurement time: 30 minutes), a suitable tracer for PET imaging, proved the basic functionality of the simulation and imaging process, achieving acceptable results for FBP and very good results using iterative image reconstruction.

Besides that, the dependence of the image quality on the number of iterations was examined (1-4 iterations, 12 subsets) and revealed an increase in image contrast turning to a higher number of iterations.

$^{90}\text{Y}$  simulations with specific activities of 4 and 40 MBq/ml and a measurement time of 30 minutes were carried out. A background activity of 0.5 MBq/ml was implemented in the 4 MBq/ml simulation.

Both simulations showed the difficulty for the usage of  $^{90}\text{Y}$  in PET imaging due to the small probability for positron emission in radioactive decay of  $^{90}\text{Y}$ .

The simulation with a specific activity of 40 MBq/ml provided acceptable image results for FBP and good results for the iteratively reconstructed image. All of the sources could be identified.

The more realistic simulation with a specific activity of 4 MBq/ml and implemented background activity showed bad results for FBP and acceptable results for the iteratively reconstructed image. The image quality is comparable with real  $^{90}\text{Y}$  PET phantom measurements.

**Outlook** In clinical routine several corrections for image reconstruction are performed. The implementation of required image corrections, like attenuation and scatter correction, that would have exceeded the complexity of this diploma thesis, will lead to an improvement in image quality. Furthermore, the realistic energy distribution of the positrons in  $^{90}\text{Y}$  decay has to be implemented.

Besides that, the import of CT and PET data from real PET measurements serving as basis for the simulation in GATE could play a role in the determination of the dose distribution in the liver of patients undergoing SIRT.

# Appendix A

## Image Reconstruction - STIR

### A.1 User Manual

For image reconstruction two algorithms were used. The FBP and the iterative OSEM algorithm.

As STIR works with sinogram data types the ROOT output files had to be modified. The following commands were used to generate projection data files from the existing ROOT files:

The C++ program from a collaborating research group from Jülich was compiled. Information on the PET scanner has to be input into the source code in order to be able to read in the data from the ROOT file:

```
g++ My_Bin_GATE.v1.0.c 'root-config -cflags -libs' -o Bin_GATE_MyPET
```

After this, the compiled C++ program was executed. The command line includes the directory name of the ROOT file, the output file name and the wanted coincidence output flag is quoted. The coincidence output flag is represented by the numbers 1 (all coincidences), 2 (true unscattered coincidences) and 3 (scatter coincidences). In general one is interested in true unscattered coincidences, so the coincidence output flag was set to 2:

```
./Bin_GATE_MyPET './.../Diplomarbeit/PET AKH/ 'Y90Sources' output_flag
```

With the command line above, the projection data file *Y90Sources.s* was generated.

For the internal processing mode of the individual image reconstruction methods in STIR a header file is required. It is pointing to the generated projection data file *Y90Sources.s*. The header file *Sinoheader\_janderl.hs* was created with the following command:

```
create_projdata_template Sinoheader_janderl
```

When executing this, STIR is asking for further information on the PET data, like the number of detector rings or the maximum ring difference which stands for the largest space between rings in potential coincidence (in 3D PET imaging the maximum ring difference is  $N - 1$ ,  $N$  standing for the number of detector rings, since all of the rings can be in coincidence).

**Filtered Back Projection** The FBP in STIR was then conducted using the command:

```
FBP2D MyFBP2D.par
```

The input of the parameter file *MyFBP2D.par* is the previously generated header file *Sinoheader\_janderl.hs*. Furthermore it contains information about FBP like the implementation of possible filters in the fourier transformation.

**Iterative Reconstruction** The intern command in STIR for executing the iterative reconstruction reads as follows:

```
OSMAPOSL My.OSMAPOSL_temp.par
```

The iterative reconstruction uses the same input file *Sinoheader\_janderl.hs* pointing to the gained simulation data and user defined PET characteristics as it is used for the FBP. More input in the parameter file *My.OSMAPOSL\_temp.par* is needed concerning the iteration adjustment like the number of iterations and the number of subsets.

# Bibliography

- [1] M. D'Arienzo. *Emission of  $\beta^+$  Particles Via Internal Pair Production in the  $0^+ - 0^+$  Transition of  $^{90}\text{Zr}$ : Historical Background and Current Applications in Nuclear Medicine Imaging*. Atoms ISSN2218, 2013.
- [2] M. Elschot, B. J. Vermolen, M. Lam, B. de Keizer, M. van den Bosch, H. de Jong. *Quantitative Comparison of PET and Bremsstrahlung SPECT for Imaging the In Vivo Yttrium-90 Microsphere Distribution after Liver Radioembolization*. PLoS ONE 8(2): e55742. doi:10.1371/journal.pone.005572, 2013.
- [3] M. K. Werner, K. Brechtel, T. Beyer, H. Dittmann, C. Pfannenberger, J. Kupferschläger. *PET/CT for the assessment and quantification of Y-90 biodistribution after selective internal radiotherapy (SIRT) of liver metastases*. J Nucl Med Mol Imaging 37:407-408, 2010.
- [4] M. Wissmeyer, S. Heinzer, P. Majno, F. Buchegger, H. Zaidi, V. Garibotto, M. Viallon, C. D. Becker, O. Ratib and S. Terraz. *Y-90 Time-of-flight PET/MR on a hybrid scanner following liver radioembolisation (SIRT)*. J Nucl Med Mol Imaging 38:1744-1745, 2011.
- [5] T. W. Barber, K. S. K. Yap and V. Kalff. *PET/CT imaging of Y-90 radiation synovectomy*. J Nucl Med Mol Imaging 39:917-918, 2012.
- [6] Y. H. Kao, J. Steinberg, J. Yan, D. W. Townsend, S. Satchithanatham, Y. S. Tay, G. Lim, P. Chow, A. Tan, D. Ng and A. Goh. *Optimization of Yttrium-90 Processing on a Clinical PET/CT System*. IEEE Nuclear Science Symposium Conference Record, 2011.
- [7] L. van Elmbt, S. Vandenberghe, S. Walrand, S. Pauwels and F. Jamar. *Comparison of yttrium-90 quantitative imaging by TOF and non-TOF PET in a phantom of liver selective internal radiotherapy*. Ohys. Med. Biol. 56, 6759-6777, 2011.

- [8] Robert Wood Johnson University Hospital. [http://www.rwjuh.edu/medical\\_services/sirt\\_spheres.html](http://www.rwjuh.edu/medical_services/sirt_spheres.html).
- [9] Radiologie Universitätsklinikum Frankfurt. [http://radiologie-uni-frankfurt.de/content/e4864/e27/e35/e9835/index\\_ger.html](http://radiologie-uni-frankfurt.de/content/e4864/e27/e35/e9835/index_ger.html).
- [10] S. Cherry, J. Sorenson and M. Phelps. *Physics in Nuclear Medicine*. Elsevier Health Sciences, 2003.
- [11] Hanno Krieger. *Grundlagen der Strahlungsphysik und des Strahlenschutzes*. B.G.Teubner Verlag, 2.Edition, 2007.
- [12] Wikipedia. [http://en.wikipedia.org/wiki/Semi-empirical\\_mass\\_formula](http://en.wikipedia.org/wiki/Semi-empirical_mass_formula).
- [13] D. L. Bailey, D. W. Townsend, P. E. Valk and M. N. Maisey. *Positron Emission Tomography Basic Sciences*. Springer London, 2005.
- [14] M. Casey and R. Nutt. *A multicrystal two dimensional BGO detector system for positron emission tomography*. IEEE Transact Nucl Sci NS 33: 460-463, 1986.
- [15] S. R. Cherry and Magnus Dahlbom. *PET: Physics, Instrumentation and Scanners*. In Michael E. Phelps: PET, Molecular Imaging and its Biological Applications, pages 1-117. Springer New York, 2006.
- [16] M. Slaney and A.C.Kak. *Principles of Computerized Tomographic Imaging*. IEEE PRESS, 1987.
- [17] L. A. Shepp and Y. Vardi. *Maximum likelihood reconstruction for emission tomography*. Medical Imaging, IEEE Transaction on, 1(2):113-122, 1982.
- [18] H. M. Hudson and R.S. Larkin. *Accelerated image reconstruction for emission tomography*. Medical Imaging, IEEE Transactions on, 13(4):601-609, 1994.
- [19] Siemens. *Biograph True Point PET System Specifications*. Technical Report, Siemens Medical Solutions, 2007.
- [20] National Electrical Manufacturers Association. *Performance Measurements of Positron Emission Tomographs*. NEMA NU 2, 2007.

- [21] S. Jan et al.. *GATE: A simulation toolkit for PET and SPECT*. Phys. Med. Biol., 49, 2004.
- [22] Medical University of Vienna. <http://www.meduniwien.ac.at/hp/moccamed/>.
- [23] R. Brun and F. Rademakers. *ROOT - An Object Oriented Data Analysis Framework*. Proceedings AIHENP'96 Workshop, Lausanne, Sep. 1996, Nucl. Inst. and Meth. in Phys. Res. A 389 81-86, 1997.
- [24] K. Thielemans et al.. *STIR: Software for Tomographic Image Reconstruction Release 2*. Physics in Medicine and Biology, 57 (4), pp. 867-883, 2012.

